The Astrophysical Journal, 977:254 (21pp), 2024 December 20 https://doi.org/10.3847/1538-4357/ad8de6

SN2023fyq: A Type Ibn Supernova with Long-standing Precursor Activity Due to Binary Interaction

Yize Dong (董一泽)[1], Daichi Tsuna[2,3], Stefano Valenti[1], David J. Sand[4], Jennifer E. Andrews[5], K. Azalee Bostroem[4,20], Griffin Hosseinzadeh[4], Emily Hoang[1], Saurabh W. Jha[6], Daryl Janzen[7], Jacob E. Jencson[8,9], Michael Lundquist[10], Darshana Mehta[1], Aravind P. Ravi[1], Nicolas E. Meza Retamal[1], Jeniveve Pearson[4], Manisha Shrestha[4], Alceste Z. Bonanos[11], D. Andrew Howell[12,13], Nathan Smith[14], Joseph Farah[12,13], Daichi Hiramatsu[15,16], Koichi Itagaki (板垣公一)[17], Curtis McCully[12,13], Megan Newsome[12,13], Estefania Padilla Gonzalez[12,13], Emmanouela Paraskeva[11], Craig Pellegrino[18], Giacomo Terreran[12,13], Joshua Haislip[19], Vladimir Kouprianov[19], and Daniel E. Reichart[19]

[1] Department of Physics and Astronomy, University of California, 1 Shields Avenue, Davis, CA 95616-5270, USA; yizdong@ucdavis.edu
[2] TAPIR, Mailcode 350-17, California Institute of Technology, Pasadena, CA 91125, USA
[3] Research Center for the Early Universe (RESCEU), School of Science, The University of Tokyo, 7-3-1 Hongo, Bunkyo-ku, Tokyo 113-0033, Japan
[4] Steward Observatory, University of Arizona, 933 North Cherry Avenue, Tucson, AZ 85721-0065, USA
[5] Gemini Observatory, 670 North A'ohoku Place, Hilo, HI 96720-2700, USA
[6] Department of Physics and Astronomy, Rutgers, the State University of New Jersey, 136 Frelinghuysen Road, Piscataway, NJ 08854-8019, USA
[7] Department of Physics & Engineering Physics, University of Saskatchewan, 116 Science Place, Saskatoon, SK S7N 5E2, Canada
[8] Department of Physics and Astronomy, Johns Hopkins University, 3400 North Charles Street, Baltimore, MD 21218, USA
[9] Space Telescope Science Institute, 3700 San Martin Drive, Baltimore, MD 21218, USA
[10] W. M. Keck Observatory, 65-1120 Māmalahoa Highway, Kamuela, HI 96743-8431, USA
[11] IAASARS, National Observatory of Athens, Metaxa & Vas. Pavlou Street, 15236, Penteli, Athens, Greece
[12] Las Cumbres Observatory, 6740 Cortona Drive, Suite 102, Goleta, CA 93117-5575, USA
[13] Department of Physics, University of California, Santa Barbara, CA 93106-9530, USA
[14] Steward Observatory, University of Arizona, 933 North Cherry Avenue, Rm. N204, Tucson, AZ 85721-0065, USA
[15] Center for Astrophysics | Harvard & Smithsonian, 60 Garden Street, Cambridge, MA 02138-1516, USA
[16] The NSF AI Institute for Artificial Intelligence and Fundamental Interactions, USA
[17] Itagaki Astronomical Observatory, Yamagata 990-2492, Japan
[18] Department of Astronomy, University of Virginia, Charlottesville, VA 22904, USA
[19] Department of Physics and Astronomy, University of North Carolina, 120 East Cameron Avenue, Chapel Hill, NC 27599, USA

Received 2024 May 8; revised 2024 October 7; accepted 2024 October 7; published 2024 December 18

Abstract

We present photometric and spectroscopic observations of SN 2023fyq, a Type Ibn supernova (SN) in the nearby galaxy NGC 4388 ($D \simeq 18$ Mpc). In addition, we trace the 3 yr long precursor emission at the position of SN 2023fyq using data from DLT40, ATLAS, Zwicky Transient Facility, ASAS-SN, Swift, and amateur astronomer Koichi Itagaki. The double-peaked postexplosion light curve reaches a luminosity of $\sim 10^{43}$ erg s^{-1}. The strong intermediate-width He lines observed in the nebular spectrum imply the interaction is still active at late phases. We found that the precursor activity in SN 2023fyq is best explained by the mass transfer in a binary system involving a low-mass He star and a compact companion. An equatorial disk is likely formed in this process ($\sim 0.6 M_\odot$), and the interaction of SN ejecta with this disk powers the second peak of the SN. The early SN light curve reveals the presence of dense extended material ($\sim 0.3 M_\odot$) at $\sim 3000 R_\odot$ ejected weeks before the SN explosion, likely due to final-stage core silicon burning or runaway mass transfer resulting from binary orbital shrinking, leading to rapid-rising precursor emission within $\sim$30 days prior to explosion. The final explosion could be triggered either by the core collapse of the He star or by the merger of the He star with a compact object. SN 2023fyq, along with SN 2018gjx and SN 2015G, forms a unique class of Type Ibn SNe, which originate in binary systems and are likely to exhibit detectable long-lasting pre-explosion outbursts with magnitudes ranging from −10 to −13.

Unified Astronomy Thesaurus concepts: Core-collapse supernovae (304); Circumstellar matter (241); Stellar mass loss (1613)

Materials only available in the online version of record: data behind figures

1. Introduction

Type Ibn supernovae (SNe) are a subclass of interaction-powered SNe that show narrow helium (He) lines but not hydrogen (H) lines in their spectra (e.g., N. Smith 2017; M. Modjaz et al. 2019). Although it has been more than two decades since the discovery of the first Type Ibn SN (SN 1999cp, T. Matheson et al. 2000), our understanding of Type Ibn progenitors remains limited. The light curves of Type Ibn SNe tend to be short lived, and some of them even resemble the evolution of fast-evolving transients (O. D. Fox & N. Smith 2019; A. Y. Q. Ho et al. 2023). A general interpretation is that SNe Ibn are Wolf-Rayet/He stars that experience enhanced mass loss right before the SN explosion.

---

[20] LSSTC Catalyst Fellow.

The interaction of SN ejecta with the surrounding dense He-rich circumstellar material (CSM) powers some of the SN light curve and ionizes the outer CSM, producing the narrow lines we observe (A. Pastorello et al. 2007; G. Hosseinzadeh et al. 2017).

Light-curve modeling of Type Ibn SNe has supported the presence of dense CSM close to the progenitors (A. Gangopadhyay et al. 2020; C. Pellegrino et al. 2022; T. Ben-Ami et al. 2023). Both SNe Ibn and their H-rich counterparts, SNe IIn, have CSM-interaction signatures that point to pre-SN mass loss that is much stronger than normal massive-star winds (N. Smith 2014, 2017). However, the mechanisms driving the enhanced mass loss near the time of explosion remain a subject of active debate. This enhanced mass loss could be attributed to the final-stage stellar activities of massive stars, where the dense CSM could be produced by eruptive outbursts through pulsational pair instability (T. Yoshida et al. 2016; S. E. Woosley 2017) or wave-driven outbursts excited by late-stage nuclear burning (E. Quataert & J. Shiode 2012; J. H. Shiode & E. Quataert 2014; J. Fuller 2017; J. Fuller & S. Ro 2018; V. Morozova et al. 2020). Alternatively, the dense CSM might be generated through binary interactions (N. Soker 2013; N. Smith & W. D. Arnett 2014; N. Smith 2014; B. D. Metzger 2022; L. Dessart et al. 2022; S. C. Wu & J. Fuller 2022; D. Tsuna et al. 2024a). In this scenario, the progenitor does not necessarily have to be a very massive star, as the mass loss would be significantly enhanced by the presence of a binary companion.

One way to constrain the progenitor of Type Ibn SNe is by searching for evidence of a massive star or a binary companion in deep images once the SN fades. For example, the low star formation rate at the site of PS1-12sk ruled out a massive-star progenitor (G. Hosseinzadeh et al. 2019). In addition, the absence of evidence for massive-star progenitors and the possible detection of binary companions have been reported for some other Type Ibn SNe (J. R. Maund et al. 2016; I. Shivvers et al. 2017).

Alternatively, a direct way to constrain the mass-loss history of SN progenitors is by searching for signs of pre-explosion activity or precursor emission prior to the SN explosion. Precursor emission is commonly observed in Type IIn SNe (e.g., N. Smith et al. 2010; J. C. Mauerhan et al. 2013; A. Pastorello et al. 2013; E. O. Ofek et al. 2013; E. O. Ofek et al. 2014; L. Tartaglia et al. 2016; A. Pastorello et al. 2018; N. L. Strotjohann et al. 2021; D. Hiramatsu et al. 2024). The bright precursor outbursts in Type IIn SNe may be due to eruptive mass loss from luminous blue variable-like progenitors (A. Gal-Yam et al. 2007; A. Gal-Yam & D. C. Leonard 2009; N. Smith 2017) or pulsational pair instability outbursts (N. Smith & R. McCray 2007; S. E. Woosley et al. 2007; N. Smith 2014). Alternatively, these outbursts could be caused by red supergiants with a compact object companion (C. L. Fryer & S. E. Woosley 1998; S. L. Schrøder et al. 2020; D. Tsuna et al. 2024a; N. Smith et al. 2024), or other late-stage binary interaction (N. Smith & W. D. Arnett 2014). To date, precursor emission has been identified in two Type Ibn SNe, SN 2006jc (A. Pastorello et al. 2007) and SN 2019uo (N. L. Strotjohann et al. 2021). The precursor outbursts in these events are shorter and fainter compared to those observed in Type IIn SNe, and have been interpreted as resulting from single massive-star activities or binary interactions (R. J. Foley et al. 2007; A. Pastorello et al. 2007; N. Smith et al. 2008; D. Tsuna et al. 2024a).

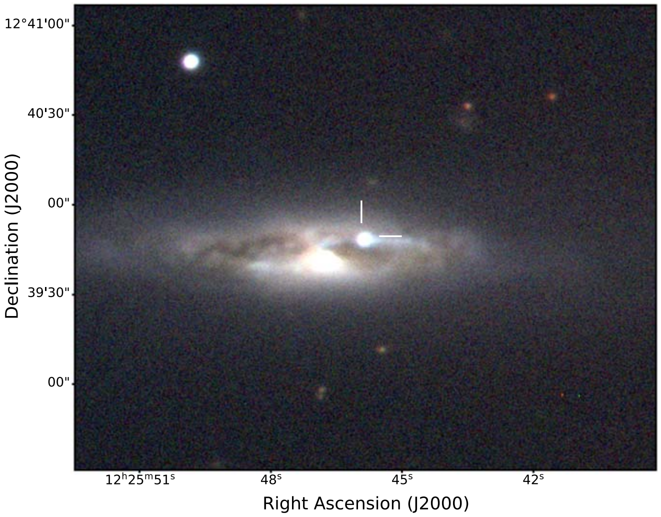

Figure 1. Composite *gri* image of SN 2023fyq in NGC 4388 obtained with the Las Cumbres Observatory on 2023 August 11. The position of SN 2023fyq is indicated by white tick markers.

In this paper, we present the optical observations of SN 2023fyq, one of the closest SNe Ibn. The light curves and spectra of this object closely resemble those of Type Ibn SNe. Notably, relatively steady precursor activity is observed up to approximately 3 yr prior to the SN explosion. The detection of precursor emission in SN 2023fyq allows us to investigate the final-stage stellar activity and the nature of its progenitor system. The pre-explosion observations of SN 2023fyq are also presented in S. J. Brennan et al. (2024), where they identify an asymmetric CSM structure, likely related to unstable stellar activities of the progenitor.

The paper is organized as follows: the photometric and spectroscopic observations are described in Section 2. We constrain the reddening and distance of SN 2023fyq in Section 3. We describe the photometric and spectroscopic evolution of SN 2023fyq in Sections 4 and 5. The progenitor scenario and the physical mechanism of precursor activities are discussed in Section 6. We summarize the main results in Section 7.

2. Observations

SN 2023fyq was discovered on 2023 April 17 by the Zwicky Transient Facility (ZTF) survey at R.A.(2000)=$12^{h}25^{m}45\overset{s}{.}847$, decl.(2000) = +12 39 48¢87 in NGC 4388 (K. De 2023; see Figure 1). On 2023 June 14, a rapid rebrightening of SN 2023fyq was observed and reported by amateur astronomer Koichi Itagaki (K. Itagaki 2023). On 2023 June 25, SN 2023fyq was classified as a peculiar Type Ib due the presence of helium lines and the lack of hydrogen lines in the optical spectrum (G. Valerin et al. 2023). As we will discuss in the paper, a Type Ibn classification is more appropriate for SN 2023fyq because its photometric and spectroscopic evolution match those of Type Ibn SNe. This is consistent with the classification of SN 2023fyq discussed in S. J. Brennan et al. (2024).

In this section, we present the photometric data of SN 2023fyq taken by Las Cumbres Observatory (T. M. Brown et al. 2013) via the Global Supernova Project, the Distance

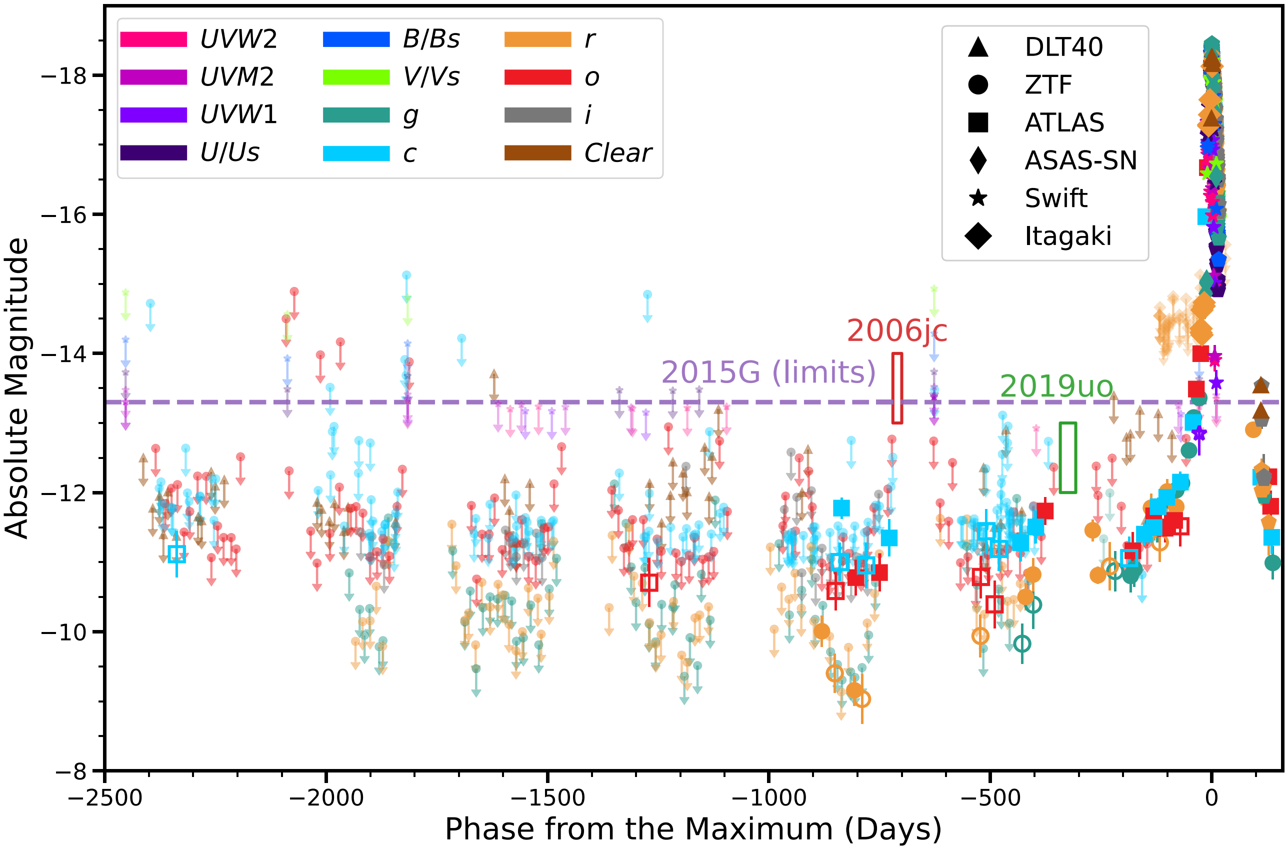

Figure 2. Photometric limits and detections of SN 2023fyq prior to and after explosion. Detections with S/N > 4 are indicated by large solid symbols, while detections with 3 < S/N ⩽ 4 are indicated by hollow symbols. The smaller symbols are nondetection limits with S/N ⩽ 3. The precursor activities detected in Type Ibn SN 2006jc (*R* band) and SN 2019uo (*r* band) are indicated in the red and green rectangles, respectively. The limits on the precursor activities on Type Ibn SN 2015G are shown with the purple dashed line. All of the bands are in the AB magnitude system.

(The data used to create this figure are available in the online article.)

Less Than 40 Mpc (DLT40; L. Tartaglia et al. 2018) survey, ZTF (E. C. Bellm et al. 2019; M. J. Graham et al. 2019), the Asteroid Terrestrial-Impact Last Alert System (ATLAS; J. L. Tonry 2011; J. L. Tonry et al. 2018; K. W. Smith et al. 2020), the All-Sky Automated Survey for Supernovae (ASAS-SN; B. J. Shappee et al. 2014; C. S. Kochanek et al. 2017), the Neil Gehrels Swift Observatory (N. Gehrels et al. 2004), and amateur astronomer Itagaki. We also report the spectroscopic follow up of SN 2023fyq taken after the SN explosion. All spectroscopic observations from this paper can be found at https://github.com/yizedong/SN2023fyq_data and will be available on WISeREP (O. Yaron & A. Gal-Yam 2012).[21]

2.1. Photometric Observations

For the photometry, we adopt a signal-to-noise ratio (S/N) threshold of 3 for source detections and an S/N threshold of 5 for computing the upper limit, following the suggestions of F. Masci (2011). The light curves are shown in Figures 2 and 3.

2.1.1. Las Cumbres Observatory Observations

Our multiband photometric follow-up campaign with Las Cumbres Observatory was initiated on 2023 July 26. The images were reduced using the PyRAF-based photometric reduction pipeline LCOGTSNPIPE (S. Valenti et al. 2016). Apparent magnitudes were calibrated using the APASS (*g*, *r*, *i*) and Landolt (*U*, *B*, *V*) catalogs.

2.1.2. DLT40 Observations

The DLT40 survey is a targeted 1 day cadence SN search for very young transients within 40 Mpc (L. Tartaglia et al. 2018; S. Yang et al. 2019).

DLT40 has been monitoring the field of SN 2023fyq since 2014 in the *Clear* filer. All of the images have been visually inspected to remove those with bad qualities. A deep template was made with the images taken between 2014 June 20 and 2015 February 1 using Swarp (E. Bertin et al. 2002). The rest of the images were stacked in windows of 15 days and were then subtracted against the template using HOTPANTS (A. Becker 2015). We used aperture photometry at the position of SN 2023fyq through a pipeline based on Photutils (L. Bradley et al. 2022). The photometry was calibrated to the *r* band.

2.1.3. ZTF Observations

ZTF is a time-domain survey using a wide-field camera mounted on the Palomar 48 inch Schmidt telescope (E. C. Bellm et al. 2019; M. J. Graham et al. 2019). The ZTF public survey searches for transients and variables in the northern sky with a 3 day cadence in *g* and *r* filters.

The position of SN 2023fyq has been monitored by ZTF since 2018. We obtained the forced photometry from the ZTF Forced Photometry Service (F. J. Masci et al. 2023). We

---

[21] https://www.wiserep.org/

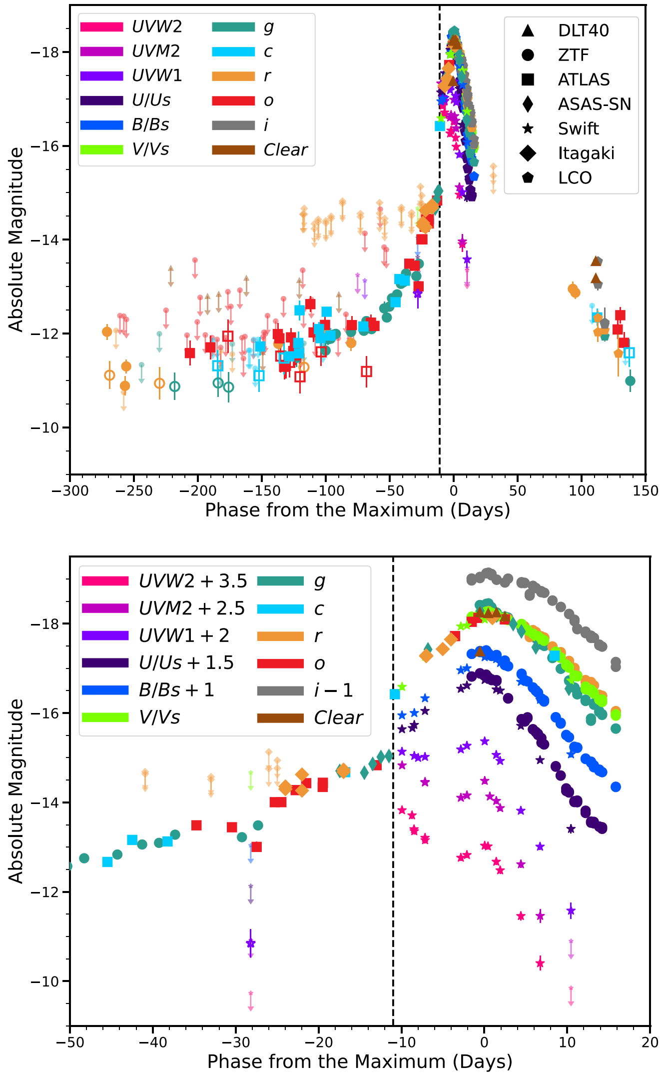

Figure 3. The light-curve evolution of SN 2023fyq. The *Clear* filter is calibrated to the r band. The hollow symbol indicates the data with $3 < \mathrm{S/N} \leqslant 4$, while the solid symbol indicates the data with $\mathrm{S/N} > 4$. Light curves in the bottom panel have been shifted by the indicated amounts to enhance clarity. All of the bands are in the AB magnitude system. The black dashed line marks the epoch of the first light of the SN (−11 days), as adopted in the paper.

removed bad-quality data following the instructions in F. J. Masci et al. (2023). For images taken after −300 days, the transient was bright enough to be detected in single images, and so, the observations were stacked in 1 day time bins. For images taken prior to −300 days, the observations were stacked in 15 day time bins to improve the S/N.

2.1.4. ATLAS Observations

The ATLAS survey is an all-sky daily cadence survey (K. W. Smith et al. 2020) carried out in two filters, cyan (c) and orange (o), roughly equivalent to Pan-STARRS filters $g + r$ and $r + i$, respectively.

The position of SN 2023fyq has been monitored by ATLAS since 2015. Forced photometry at the SN position was obtained from the ATLAS forced photometry server (L. Shingles et al. 2021). Using the method presented in D. Young (2022), we stacked the measurements to improve the S/N and obtain deeper upper limits. For images taken after −300 days, the observations were stacked in 1 day time bins. For images taken before −300 days, the observations were stacked in 15 day time bins.

2.1.5. ASAS-SN Observations

ASAS-SN is an untargeted all-sky survey to a depth of $g{\sim}18.5$ mag (B. J. Shappee et al. 2014; C. S. Kochanek et al. 2017). We obtained the ASAS-SN reference image subtracted forced photometry from the ASAS-SN sky portal.[22]

2.1.6. Swift Observations

The position of SN 2023fyq has been observed by the UVOT instrument on the Neil Gehrels Swift Observatory (N. Gehrels et al. 2004) since 2015. We performed aperture photometry with an aperture size of 3″ at the position of SN 2023fyq on Swift UVOT images using the High-Energy Astrophysics software. Background variations in individual images were removed using a 5″ aperture placed on a blank section of the sky. To remove the underlying galaxy background contamination, we subtracted the flux extracted from Swift UVOT images taken on 2016 November 8. Zero-points were chosen from A. A. Breeveld et al. (2011) with time-dependent sensitivity corrections updated in 2020.

2.1.7. Koichi Itagaki's Observations

We also incorporated observations taken with Koichi Itagaki's Bitran BN-83MCCD imager mounted on a 0.5 m telescope in Okayama Prefecture, Japan. We solved the astrometry of the images using Astrometry.net (D. Lang et al. 2010). The aperture photometry was performed using a pipeline based on Photutils (L. Bradley et al. 2022) and was calibrated to r-band magnitudes in the Sloan system (M. Fukugita et al. 1996).

2.2. Spectroscopic Observations

We collected four optical spectra from the FLOYDS spectrograph (T. M. Brown et al. 2013) on the 2 m Faulkes Telescope South in Australia at the Las Cumbres Observatory via the Global Supernova Project. The FLOYDS spectra were reduced following standard procedures using the FLOYDS pipeline (S. Valenti et al. 2014). We triggered Gemini-North Target of Opportunity (ToO) observations with the Gemini Multi-Object Spectrograph (GMOS; I. M. Hook et al. 2004) and the B600 grating on 2023 July 27 and 2023 August 1 through proposal GN-2023A-Q-136. The Gemini spectra were reduced by using the IRAF Gemini package. We triggered further ToO observations with the Andalucia Faint Object Spectrograph and Camera (ALFOSC) on the Nordic Optical Telescope (NOT) at the Spanish "Roque de los Muchachos" Observatory on 2023 August 4 through proposal 67-112. The NOT ALFOSC spectrum was observed using Grism #4 and a 1.″0 slit and was reduced using the PypeIt pipeline (J. Prochaska et al. 2020; J. X. Prochaska et al. 2020). We obtained spectra on 2023 December 12 and 2024 May 1 from the Low-Resolution Imaging Spectrometer (LRIS; J. B. Oke et al. 1995) on the Keck I telescope. The LRIS spectra were reduced in a standard way using the LPipe pipeline (D. A. Perley 2019). A low-resolution spectrum was taken on 2024 January 23 with the Goodman High Throughput Spectrograph (GHTS) on the

---

[22] https://asas-sn.osu.edu/

Southern Astrophysical Research Telescope (SOAR; J. C. Clemens et al. 2004), and was reduced with the Goodman pipeline (S. Torres et al. 2017). One spectrum was obtained with the Multi-Object Double Spectrographs (MODS; R. W. Pogge et al. 2010) on the twin 8.4 m Large Binocular Telescope (LBT) at Mount Graham International Observatory. The spectrum was reduced using standard techniques, including bias subtraction and flat-fielding using the MODSCCDred package (R. Pogge 2019) and further reduced with IRAF including cosmic-ray rejection, local sky subtraction, and extraction of one-dimensional spectra. A log of the spectroscopic observations is presented in Table C1. We also present an unpublished nebular spectrum of Type Ibn SN 2019kbj taken at 80 days after the peak. The spectrum was taken on 2019 September 23 with the DEep Imaging Multi-Object Spectrograph (DEIMOS; S. M. Faber et al. 2003) on the Keck II telescope (Table C1). The DEIMOS spectrum was reduced using the PypeIt pipeline (J. Prochaska et al. 2020; J. X. Prochaska et al. 2020). A detailed analysis of SN 2019kbj has been presented in T. Ben-Ami et al. (2023).

3. Observational Properties

3.1. Reddening

The empirical correlation between the equivalent width (EW) of the Na I D line and the amount of gas and dust along the line of sight has often been used in extinction estimations (U. Munari & T. Zwitter 1997). In order to measure the line-of-sight reddening toward SN 2023fyq, we analyzed the medium-resolution spectrum (R∼1800) taken with Gemini North on 2023 August 1. The measured EW of the host-galaxy Na I D $\lambda5890$ (D_2) and Na I D $\lambda5896$ (D_1) are 0.27 ± 0.04 Å and 0.15 ± 0.04 Å, respectively. The measured EW of the Galactic Na I D_2 and Na I D_1 are 0.23 ± 0.02 Å and 0.16 ± 0.01 Å respectively. Using Equation (9) in D. Poznanski et al. (2012) and applying the renormalization factor of 0.86 from E. F. Schlafly et al. (2010), we found a host extinction of $E(B-V)_{\mathrm{host}} = 0.037 \pm 0.09$ mag. The Milky Way extinction is measured to be $E(B-V)_{\mathrm{MW}} = 0.035 \pm 0.09$ mag, which is consistent with the Milky Way extinction of $E(B-V)_{\mathrm{MW}} = 0.0286$ mag from the extinction map by E. F. Schlafly & D. P. Finkbeiner (2011). We adopt the latter for the Milky Way extinction. Throughout the paper, we will adopt a total extinction of $E(B-V)$=0.066 ± 0.09 mag.

We note that S. J. Brennan et al. (2024) found a larger host extinction value ($E(B-V)_{\mathrm{host}} = 0.4 \pm 0.1$ mag) using the Balmer ratio measured from the host emission lines. The disagreement is probably because this method measures the full column of gas including the background. In this case, there is likely some dust between the SN and the underlying HII region, which is responsible for this greater implied extinction value.

3.2. Distance

The distance of NGC 4388 listed on the NASA/IPAC Extragalactic Database (NED) ranges from 13.6–25.7 Mpc ($\mu = 30.67$–32.05 mag). We adopt the most recent Tully–Fisher distance (based on photometry at 3.6 μm with Spitzer Space Telescope), 18.0 ± 3.7 Mpc ($\mu = 31.28 \pm 0.45$ mag; R. B. Tully et al. 2016).

4. Photometric Evolution

In Figure 2, we present the photometric evolution of SN 2023fyq dating back to 2015, illustrating our search for precursor activities. In Figure 3, we take a closer look at the evolution from 1 yr before the SN explosion. All phases mentioned in the paper are with respect to the maximum light in the r band, which is measured to be at JD = $2{,}460{,}154.3 \pm 0.5$ after fitting the light curve with a spline function. At ∼−11 days, a sudden rise of ∼1.5 mag within ∼17 hr is clearly observed (see lower panel of Figure 3). As we will discuss below, we attribute this rapid rise to the SN first light. Consequently, we divide the photometric evolution of SN 2023fyq into two phases: the precursor phase (<−11 days) and the SN phase (>−11 days).

4.1. Precursor Detections

The precursor is detected from ∼−1000 to ∼−11 days. There are also single detections at around −2300 and −1300 days. These detections have $3 < \mathrm{S/N} \leqslant 4$, and are bracketed by nondetections of similar depth. Therefore, they are likely not true detections of precursor emission. As illustrated in Figure 2, the precursor activities remain relatively stable at −10 to −12 mag between ∼ −1300 and ∼ −100 days. Then, starting from −100 days, the object slowly brightens to ∼−15 mag. Between ∼−2500 and ∼−100 days, the UV observations from Swift only give nondetection limits (see Figure 2). As the precursor gets brighter, at ∼−28 days, a source is detected in the $UVW1$ filter at ∼−13 mag, with similar magnitudes observed in g and o bands. From −300 to −11 days, the precursor light curves seem to exhibit multiple bumps, indicative of pre-explosion activities, such as small eruptions, from the progenitor star. As shown in Figure 2, the precursor emission detected in SN 2023fyq appears fainter and longer compared to that observed in Type Ibn SN 2006jc (A. Pastorello et al. 2007) and SN 2019uo (N. L. Strotjohann et al. 2021), even when accounting for uncertainties in the distance measurement of SN 2023fyq. Pre-explosion activities were not detected for Type Ibn SN 2015G down to -13.3 ± 0.5 mag (I. Shivvers et al. 2017). It should be noted that the precursor searches for SN 2006jc and SN 2019uo only go down to around −13 mag. Therefore, fainter precursor activities like those observed in SN 2023fyq cannot be excluded for these events.

4.2. SN Light Curve

The bluer-band ($UVW2$, $UVM2$, $UVW1$) light curves of SN 2023fyq exhibit a notable bump from −11 to −4 days, before reaching the second peak and then falling off rapidly. This initial bump in the blue bands is likely attributable to the cooling following shock breakout (SBO). For the rest of the bands, the SN light curves show a fast rise and also a fast decline. The peak r-band magnitude is measured to be $M_r = -18.5$ mag. In Figure 4, we compare the r-band light curve of SN 2023fyq with the r/R-band light curves of a sample of Type Ibn SNe and well-studied normal stripped-envelope SNe (SESNe). At early times, SN 2023fyq appears more luminous than the typical SESNe, and the evolution of SN 2023fyq is overall similar to those of Type Ibn SNe. At late times, SN 2023fyq declines similarly to SN 2018gjx and SN 2015G, but slower than SN 2006jc. The steep decline of SN 2006jc in the optical is likely due to dust formation in the SN ejecta or in the surrounding CSM (e.g., N. Smith et al. 2008). The slower decline of SN 2023fyq, SN 2018gjx, and

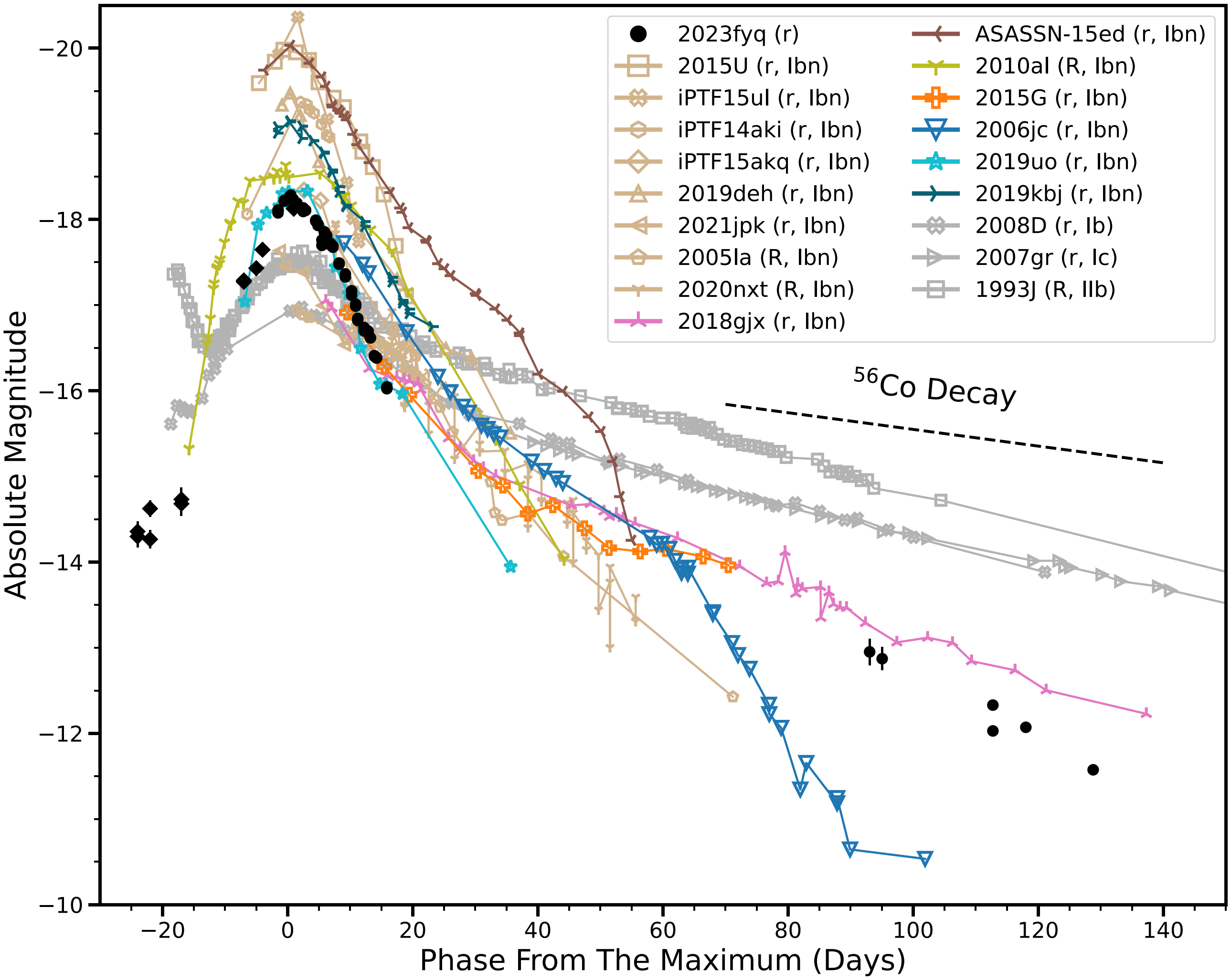

Figure 4. r/R light-curve comparison between SN 2023fyq, a sample of Type Ibn SNe, and well-studied normal SESNe. The Vega magnitudes have been converted to the AB magnitude system. The evolution of SN 2023fyq is similar to those of Type Ibn SNe. The SNe used in this plot includes Type IIb SN 1993J (A. V. Filippenko et al. 1993), Type Ib SN 2008D (M. Modjaz et al. 2009), Type Ic SN 2007gr (D. J. Hunter et al. 2009), and Type Ibn SNe: SN 2015U (A. Pastorello et al. 2015a; D. Y. Tsvetkov et al. 2015; G. Hosseinzadeh et al. 2017), iPTF15ul (G. Hosseinzadeh et al. 2017), iPTF14aki (G. Hosseinzadeh et al. 2017), iPTF15akq (G. Hosseinzadeh et al. 2017), SN 2019deh (C. Pellegrino et al. 2022), SN 2021jpk (C. Pellegrino et al. 2022), SN 2005la (A. Pastorello et al. 2008a), SN 2020nxt (Q. Wangq et al. 2024), SN 2018gjx (S. J. Prentice et al. 2020), ASASSN-15ed (A. Pastorello et al. 2015b), SN 2010al (A. Pastorello et al. 2015c), SN 2015G (G. Hosseinzadeh et al. 2017; I. Shivvers et al. 2017), SN 2006jc (A. Pastorello et al. 2007), SN 2019uo (A. Gangopadhyay et al. 2020), and SN 2019kbj (T. Ben-Ami et al. 2023). SN 2018gjx, ASASSN-15ed, SN 2010al, SN 2015G, SN 2006jc, SN 2019uo, and SN 2019kbj will be used for further comparison in the paper, while a broader sample of SNe Ibn are shown in tan. SESNe are shown in gray.

SN 2015G at late times could be an indication of less efficient dust formation than in SN 2006jc. However, due to the lack of late-phase observations of Type Ibn SNe, it is not clear if SN 2006jc is really an outlier. SN 2023fyq declines faster than normal SESNe at nebular phases. This may be due to an inefficient trapping of gamma rays in SN 2023fyq if the light-curve tail is powered by ^{56}Ni decay, a power source other than ^{56}Ni decay, or dust formation in SN 2023fyq.

4.3. Bolometric Light Curve

We constructed the bolometric light curve of SN 2023fyq using data from ZTF, ATLAS, ASAS-SN, Swift, and Itagaki. Since our photometry data come from different sources, the observations may not have been taken simultaneously. To build the spectral energy distribution (SED) in the regions without complete multiband coverage, we reconstruct the multiband light curves using the light-curve fitting package presented in M. Demianenko et al. (2023). This method is able to capture correlations across different observations over time and among various passbands, and compute an approximate light curve within the specified time and wavelength ranges. We have examined different light-curve approximation methods presented in M. Demianenko et al. (2023) and found that the results are not sensitive to the choice of method. We do not extrapolate beyond the observed bands and time frames. The final bolometric light curve is calculated by fitting the SED with a blackbody function using a Markov Chain Monte Carlo (MCMC) routine in the Light Curve Fitting package (G. Hosseinzadeh & S. Gomez 2020). For the pre-explosion phase, the temperature cannot be well constrained because there are only three or four bands of data available. Therefore, the blackbody temperatures measured from the pre-explosion spectra of SN 2023fyq in S. J. Brennan et al. (2024), after correcting the reddening using the value in our paper, are used as priors for the SED fitting for the precursor phase. This will help constrain the temperature and luminosity evolution during

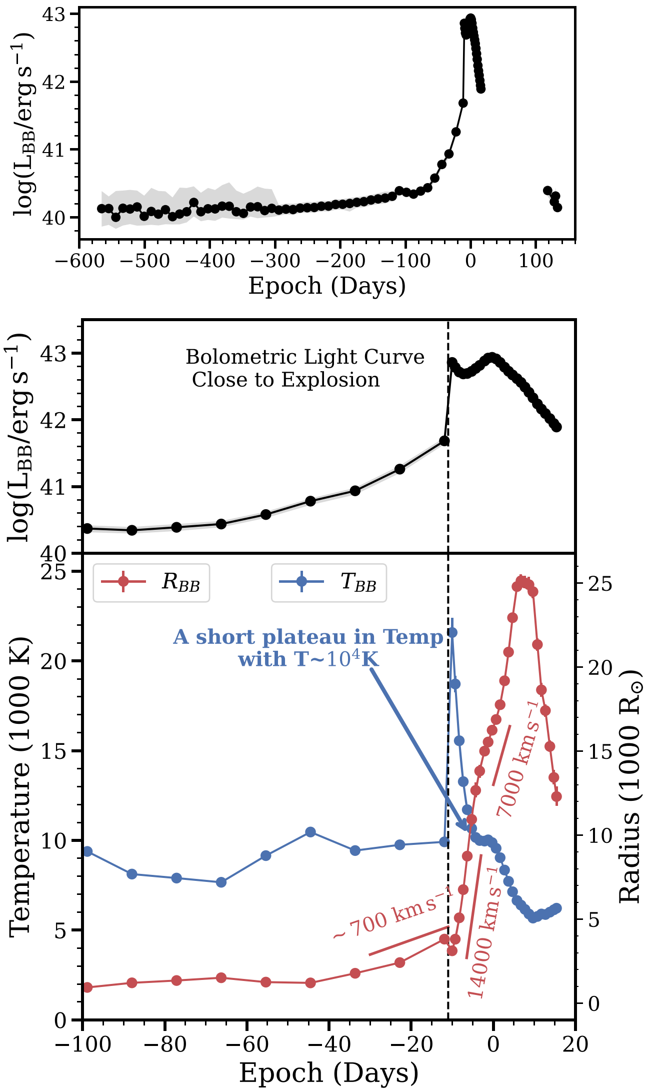

Figure 5. The pre and postexplosion bolometric light curve (upper two panels) and the blackbody temperature and radius evolution (bottom panel) of SN 2023fyq at the precursor phases and the early SN phases. The uncertainties are indicated by the shaded area.

(The data used to create this figure are available in the online article.)

the pre-explosion phase. We present the bolometric light curve of SN 2023fyq, and the corresponding blackbody temperature (T_{BB}) and radius (R_{BB}), in the precursor phase and the SN phase, in Figure 5. We note that we only focus on the long-term evolution of the bolometric light curve, and small variations in the light curves are not reflected in the final bolometric light curve.

Before ~ -100 days, the precursor of SN 2023fyq is in a relatively stable state with a luminosity of $\sim 1 \times 10^{40}$ erg s^{-1}. During that time, T_{BB} and R_{BB} are around 10,000 K and 600 $R_\odot$, respectively. After −100 days, SN 2023fyq shows a faster rise, and, at ~ -11 days, the luminosity suddenly increases over an order of magnitude (i.e., from $\sim 4 \times 10^{41}$ erg s^{-1} to $\sim 7 \times 10^{42}$ erg s^{-1}). Later, after a brief decline, the SN reaches its second peak and declines afterwards. The decline of luminosity shortly after ~ -11 days is likely due to the shock cooling after the SBO. For T_{BB}, after jumping to ∼22,000 K at ~ -11 days, it rapidly declines until entering a brief plateau phase between ~ -5 and 0 days with $T_{BB} \simeq 10{,}000$ K. The color evolution of SN 2023fyq also shows a plateau around this phase (see Appendix A), indicating that the temperature plateau is not an artificial feature caused by the interpolation method used. After around −40 days, R_{BB} shows a gradual expansion with a velocity of ∼700 km s^{-1}. After −11 days, R_{BB} continuously increase, reflecting an increase of the photospheric radius with the expansion of SN ejecta. The expansion rate of R_{BB} is ∼14,000 km s^{-1} initially, which slows down to ∼7000 km s^{-1} after around –2 days. We note that this change in photospheric velocity could also be attributed to geometric effects. After around 5 days, as will be discussed in the next section, the spectra of SN 2023fyq are dominated by absorption lines from the SN ejecta, so R_{BB} may not accurately reflect the position of the photosphere. We note that this may also influence the accuracy of the bolometric luminosity we obtained.

5. Spectroscopic Evolution

The spectroscopic evolution of SN 2023fyq is presented in Figure 6. At –1.6 days, the spectrum shows a blue continuum with a prominent He I λ5876 line. Other He lines, such as He I λ5015, He I λ6678, He I λ7065, and He I λ7281, are also observed. The He I λ5876 line shows a rather asymmetric profile (right panel of Figure 6). In the blue wing, the He I λ5876 line shows a two-component profile, with a narrow absorption feature at ~ -1000 km s^{-1} and a broad absorption feature at ~ -7000 km s^{-1}. The velocities reported here come from the absorption minimum. The detection of a two-component He I line profile in SN 2023fyq is consistent with those observed in other Type Ibn SNe (A. Pastorello et al. 2016), and is likely from different emitting regions. The broad component is from the fast moving ejecta, while the narrow component is likely from the surrounding unshocked He-rich CSM. In the red wing, there is an additional emission component peaking at around 1500 km s^{-1}. This component is also observed during the pre-explosion phase of SN 2023fyq (S. J. Brennan et al. 2024), and could be due to an asymmetric CSM structure formed before the SN explosion. A few days later, the object quickly becomes redder, and the Ca II H&K λλ3934, 3969 and Ca II λλ 8498, 8542, 8662 lines appear more prominent. No broad hydrogen features are observed in the spectra of SN 2023fyq. However, we cannot exclude the presence of narrow hydrogen lines since the spectra are heavily contaminated by the host-galaxy emission. At ∼137 days, the spectrum is dominated by strong [O I] λλ 6300, 6364 and [Ca II] λλ 7291, 7323. He lines, such as He I λ5876 and He I λ7065, are also strong at this phase. Other lines, including Mg I] λ4571 and Ca II λλ 8498, 8542, 8662, can be seen in the spectrum. After that, the spectra we have are mainly dominated by the host, while weak [O I] λλ 6300, 6364 lines are still present.

We compare the spectra of SN 2023fyq around 0 and 7 days with other SNe Ibn and normal SESNe at similar phases in Figures 7 and 8. At around 0 days, other SNe Ibn show blue continua plus narrow He I λ5876 lines in their spectra. The velocities of those narrow He I λ5876 lines are consistent with that of the narrow component of the He I λ5876 line in SN 2023fyq. At around 0 days, normal SESNe are redder than SN 2023fyq and other SNe Ibn. This is probably due to the presence of CSM in the SNe Ibn, which is not significant in SESNe. SESNe start to show lines from iron-group elements at this phase, whereas these features are not strong in SN 2023fyq or other SNe Ibn at a similar phase. This is likely due to

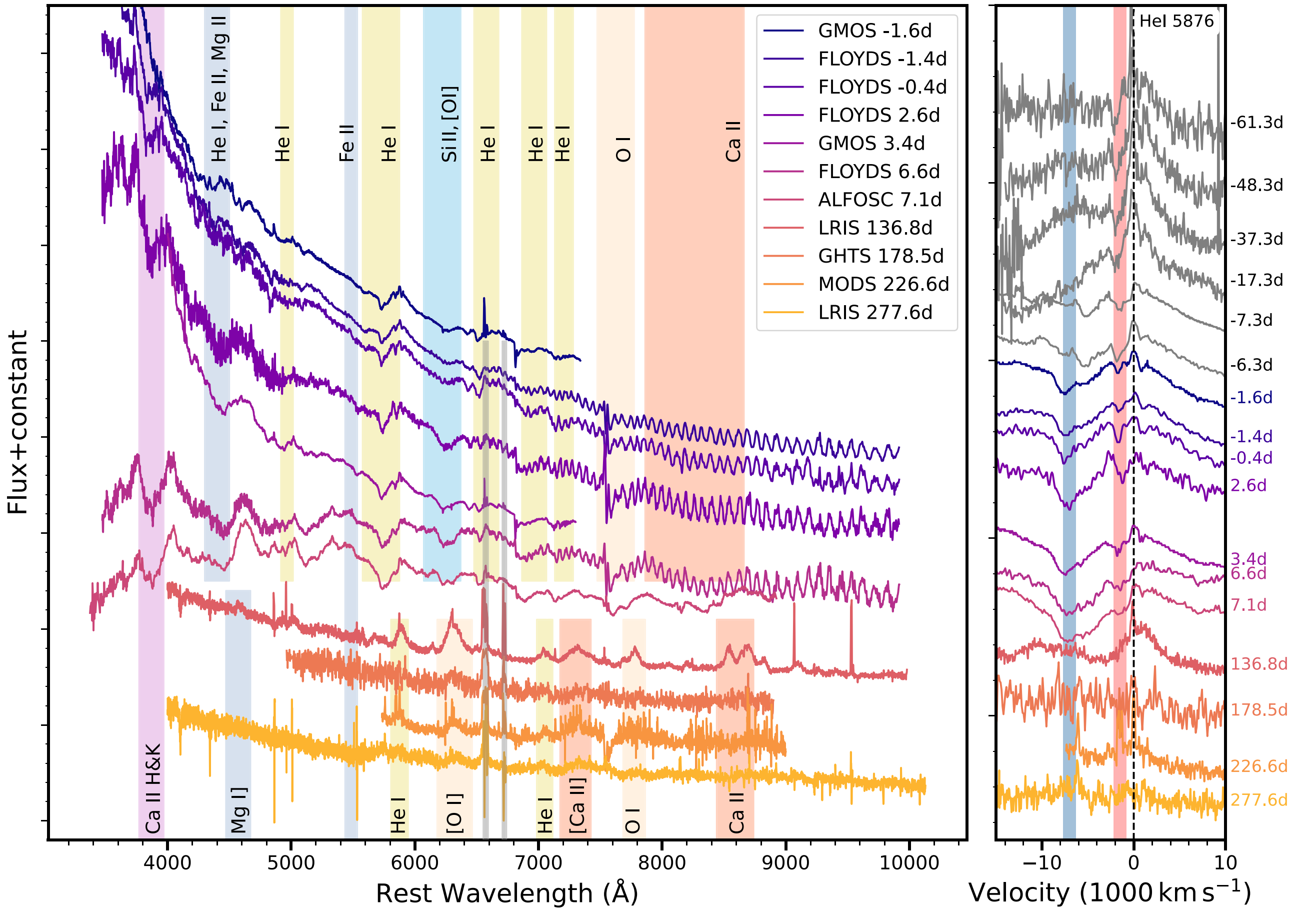

Figure 6. Left: The optical spectroscopic evolution of SN 2023fyq. The phase is measured from the *r*-band maximum. The gray bands mark the emission lines from the galaxy. Right: The evolution of the He I λ5876 line. The premaximum spectra marked in gray are from S. J. Brennan et al. (2024). The He I λ5876 line shows a high-velocity component (marked with the blue band) and a low-velocity component (marked with the red band), which may come from the SN ejecta and He-rich CSM, respectively.

(The data used to create this figure are available in the online article.)

SN 2023fyq having a hotter photosphere at this phase compared to other SESNe. The He lines in Type Ib/c SNe are also much broader than those shown in SN 2023fyq.

At around 7 days, SN 2023fyq is very similar to SNe Ibn SN 2018gjx, ASASSN-15ed, SN 2010al, and SN 2015G, which start to show signatures from deeper layers of the ejecta. The He I λ5876 lines of SN 2018gjx, ASASSN-15ed, SN 2010al, and SN 2015G grow broader, with velocities similar to that of the broad component of He I λ5876 in SN 2023fyq. Interestingly, some similarities between SN 2023fyq and normal SESNe are also observed at around 7 days. To better illustrate this, we flatten the spectrum of SN 2023fyq at ~7 days using SNID following the procedure outlined in S. Blondin & J. L. Tonry (2007) and compare the flattened spectrum with Type Ib and Ic templates at 10 days from Y.-Q. Liu et al. (2016) in the bottom panel of Figure 8. This comparison clearly indicates that SN 2023fyq exhibits spectral features similar to those of Type Ic SNe, suggesting that its progenitor likely involves a stripped/He star.

When the object enters the nebular phase, the ejecta become optically thin, providing a unique opportunity to study the core of the progenitor star. However, it is challenging to follow up SNe Ibn at nebular phases since they rapidly get fainter. In Figure 9, we compare the nebular spectrum of SN 2023fyq at ~136.8 days with a few SNe Ibn with late-time observations and normal SESNe at similar phases. The underlying continuum of the background galaxy, obtained from a pre-explosion spectrum taken at -504 days as presented in S. J. Brennan et al. (2024) when the signal from the host is dominant, is subtracted from the spectrum presented here. SN 2023fyq shows strong intermediate-width He emission lines (full width at half-maximum velocity of ~4000 km s^{-1}), similar to Type Ibn SN 2018gjx and SN 2015G, but the [O I] λλ 6300, 6364 line in SN 2023fyq is significantly stronger than those in other objects. Type Ibn SN 2006jc shows only narrow He lines with no signatures of oxygen. SN 2019kbj is overall similar to SN 2006jc but has broader He lines. This is likely because the spectrum of SN 2019kbj presented here is at an earlier phase (80 days). As shown in A. Pastorello et al. (2008b), the He lines in SN 2006jc became narrower over time. Given the overall similarities between SN 2006jc and SN 2019kbj, we expect the He lines in SN 2019kbj to also become narrower at later phases. SNe Ibn at nebular phases ($\gtrsim$100 days) seem to fall into two distinct classes, with one still showing only narrow lines and another showing intermediate-width He lines and oxygen lines. Compared to normal SESNe SN 2008D and SN 2007gr, SN 2023fyq shows prominent He emission lines, but otherwise, SN 2023fyq is similar to those normal SESNe at the nebular phase.

Overall, the spectroscopic evolution SN 2023fyq is similar to those of some SNe Ibn. However, the difference between SESNe and SN 2023fyq shortly after the light-curve maximum

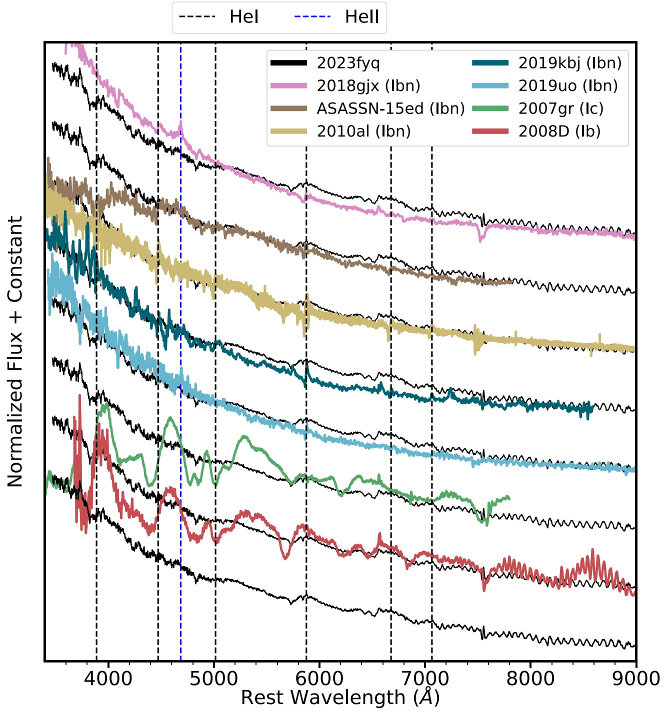

Figure 7. Optical spectral comparison of SN 2023fyq at $\sim$0 days to other Type Ibn SNe and normal SESNe.

is less evident. A transition between Type Ibn and Type Ic is clearly observed. Similar behaviors have been reported in several previous studies of other Type Ibn SNe (e.g., A. Pastorello et al. 2015b; S. J. Prentice et al. 2020). If SN 2023fyq is indeed dominated by CSM interaction at peak light, the transition to Type Ic could be due to the CSM-interaction region becoming transparent over time, allowing us to see more signatures from the SN ejecta. It is also possible that the SN ejecta has moved beyond the dense CSM. This suggests that SN 2023fyq is likely exploded from a stripped/He star within He-rich CSM. The He lines observed at the nebular phase indicate that the interaction with the He-rich CSM is still ongoing. It is natural to link the preexisting He-rich CSM with the pre-explosion activities of the progenitor system, which likely also produces the precursor emission observed in SN 2023fyq. This topic will be further discussed in Section 6.3.

6. Discussions

The detection of sustained precursor emission in SN 2023fyq provides an invaluable opportunity to study the progenitor system of Type Ibn SNe. Below is a summary of the primary observed characteristics of SN 2023fyq:

1. a long-standing and continuously rising precursor emission starting from years before the SN explosion;
2. the light curve following the explosion exhibits an evolution similar to Type Ibn SNe; the bolometric light curve exhibits two peaks;
3. the early phase and late-phase spectra both show narrow/intermediate-width He lines; the nebular spectra show prominent [O I] $\lambda\lambda$ 6300, 6364 emission, suggesting that SN 2023fyq is likely a stripped/He star exploded within He-rich CSM.

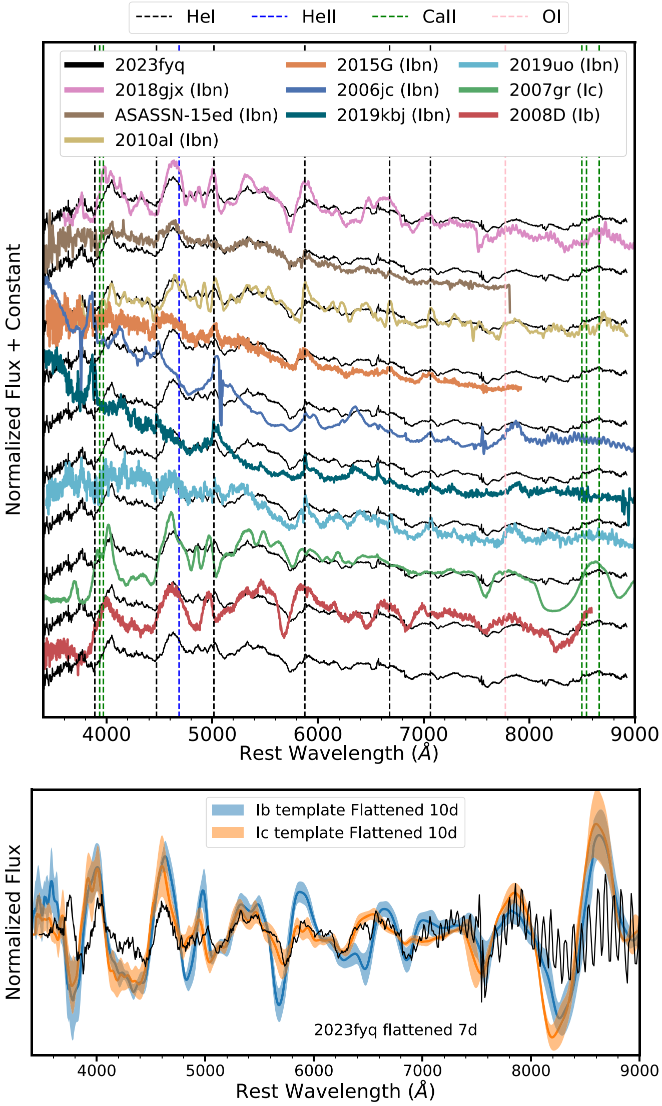

Figure 8. Upper: Optical spectral comparison of SN 2023fyq at $\sim$7 days to other Type Ibn SNe and normal SESNe. Bottom: The optical spectrum taken at $\sim$7 days compared to the mean spectra (the solid lines) and the standard deviations (the shaded regions) of SN Ib and Ic at $\sim$10 days from Y.-Q. Liu et al. (2016). SN 2023fyq has several features in common with these normal SESNe, suggesting the progenitor of SN 2023fyq involves a stripped star.

Any progenitor scenario for SN 2023fyq needs to explain the above behaviors. In this section, we will discuss the progenitor system and possible powering mechanisms of the precursor and the SN light curve.

6.1. What Powers the First Peak of the SN Bolometric Light Curve?

The light curve of SN 2023fyq reaches its initial peak at around -11 days. The later decrease of luminosity is associated with a prompt decline of T_{BB} and a rapid expansion of R_{BB}. This process is likely the shock cooling phase after the SBO. At the beginning of this phase, the expansion of the ejecta is nearly adiabatic, converting the thermal energy into kinetic energy. The rapid decline of the photospheric temperature can produce a decrease in brightness in bluer bands and an increase in brightness in redder bands as the temperature moves through the optical bands, which is consistent with what we see in SN 2023fyq (Figure 3). It is noteworthy that, around the SBO,

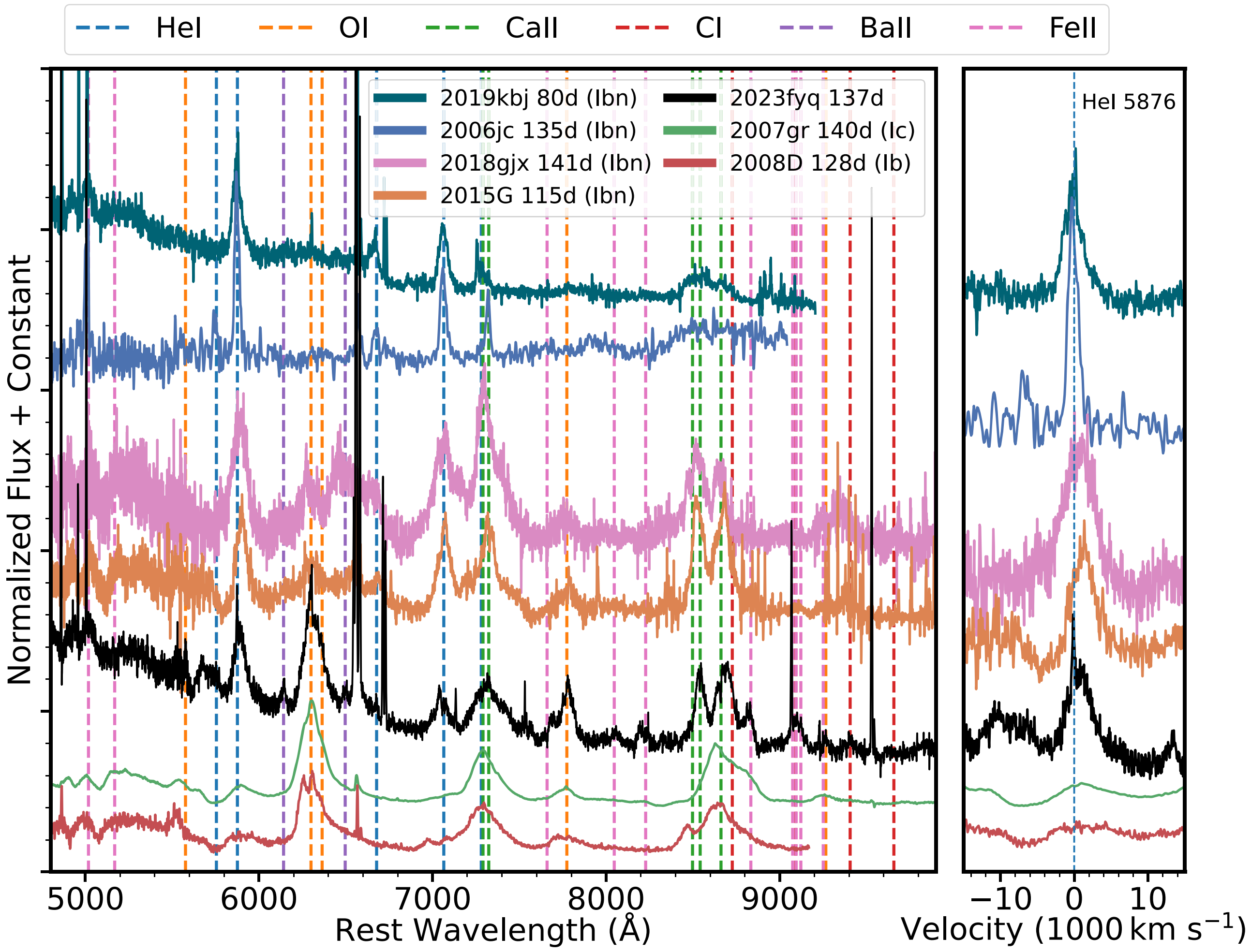

Figure 9. Left: Nebular spectral comparison of SN 2023fyq to other Type Ibn SNe with nebular spectra and normal SESNe. The phases are relative to the time of maximum light. A continuum spectrum of the background galaxy is subtracted from the spectrum of SN 2023fyq. At nebular phases, SNe Ibn appear to fall into two distinct classes: one exhibiting only narrow He lines (SN 2019kbj and SN 2006jc), and another displaying intermediate-width He lines and oxygen lines (SN 2023fyq, SN 2015G, and SN 2018gjx). Right: the evolution of the He I $\lambda5876$ line.

R_{BB} is about $3 \times 1000\,R_\odot$ ($\sim 2\times10^{14}$ cm), so the SBO likely originates from an extended envelope/CSM wind instead of from the stellar surface. A similar conclusion is also drawn by S. J. Brennan et al. (2024) based on the pre-explosion spectroscopic and photometric observations of SN 2023fyq.

When T_{BB} drops down to $\simeq$10,000 K, it enters a brief plateau phase (Figure 5). Meanwhile, the bolometric light curve reaches the second peak. This T_{BB} plateau phase is likely due to the emergence of another energy source. It is also possible that this T_{BB} plateau phase is partially due to the recombination of He I, and the decrease of R_{BB} expansion rate is due to the recession of the photosphere into the extended envelope. After this process, the outer envelope becomes almost transparent due to the drop of electron scattering opacity. This is consistent with the fact that we start to see more signals, such as Ca lines, from the deeper SN ejecta after 0 day.

In conclusion, the first peak of the SN bolometric light curve of SN 2023fyq is likely due to SBO in an extended envelope/CSM wind located at $\sim$2000–3000 $R_\odot$.

6.2. What Powers the Second Peak of the SN Bolometric Light Curve?

At 0 days, SN 2023fyq reaches its second peak. It should be noted that all bands (from UV to optical) show peaks at this phase, so this second peak is not an effect of temperature evolution and is instead powered by other formats of energy sources.

6.2.1. Radioactive Decay?

We first consider the possibility that the SN light curve around the second peak is powered by the ^{56}Ni decay. The early light-curve evolution of SNe is regulated by the photon diffusion time, which depends on the SN ejecta mass, the ejecta velocity, and the opacity (W. D. Arnett 1982). Assuming that the rise time of the light curve is equal to the photon diffusion time and Arnett's law holds for this object, i.e., the peak luminosity is close to the instantaneous decay power at the peak, we can estimate the ^{56}Ni mass ($M_{\rm Ni}$) and the ejecta mass ($M_{\rm ej}$). We fix the optical opacity $\kappa_{\rm opt}$ to be 0.1 cm^2 g^{-1}. Given a peak luminosity of 9.5×10^{42} erg s^{-1}, we get $M_{\rm Ni} \simeq 0.28\,M_\odot$ and $M_{\rm ej} \simeq 0.54 M_\odot (v_{ph}/7000\ {\rm km\,s^{-1}})({\rm t}/10\ {\rm days})^2$.

Therefore, to power the light curve with only ^{56}Ni decay, around half of the ejecta is composed of ^{56}Ni. This ratio is much higher than those in typical CCSNe (e.g., J. D. Lyman et al. 2016) and similar to those found in Type Ia SNe (e.g., R. Könyves-Tóth et al. 2020; M. L. Graham et al. 2022). If the ejecta is ^{56}Ni rich, when the ejecta become optically thin, the optical spectra would be dominated by forbidden lines from

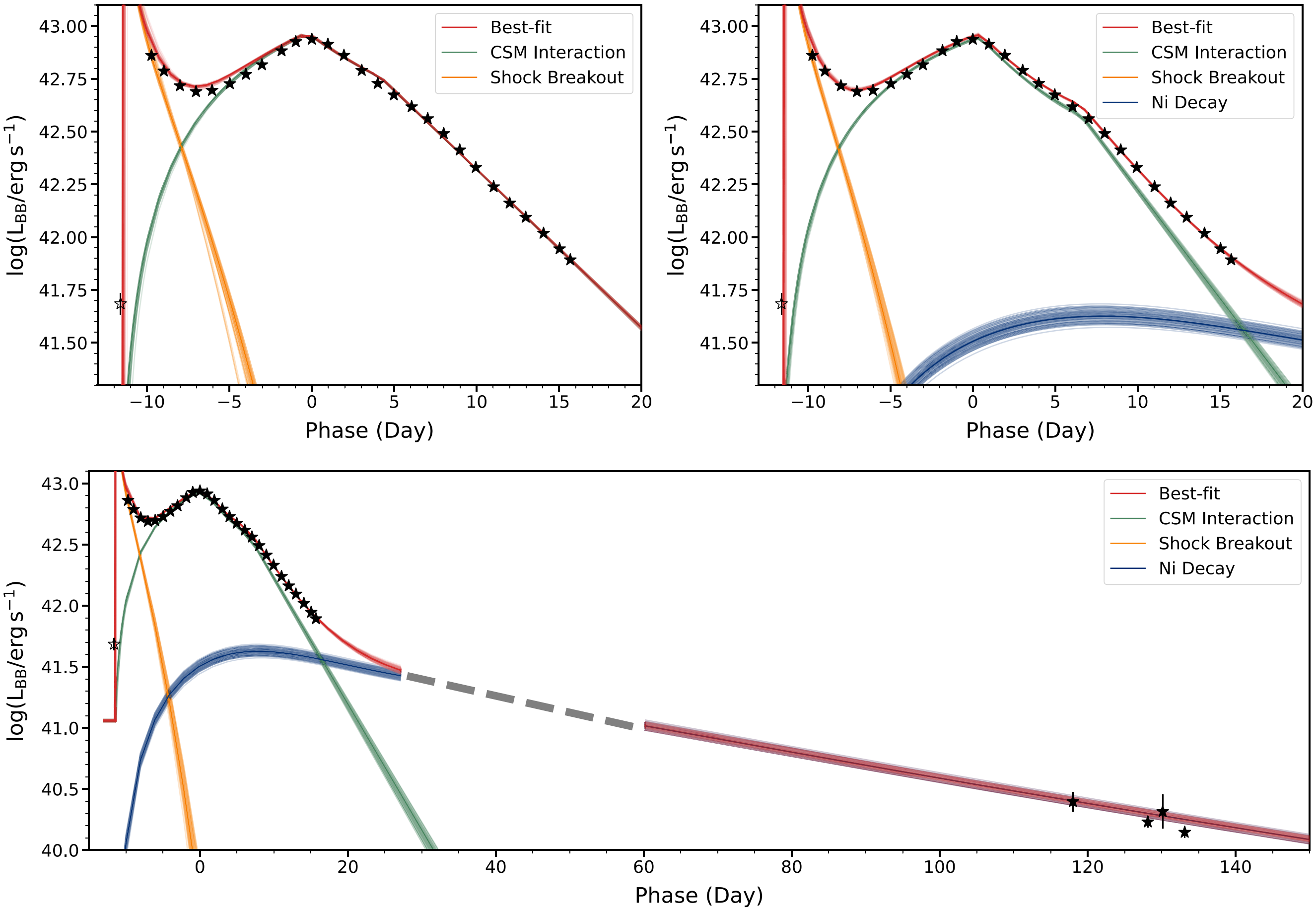

Figure 10. Upper left: fits to the bolometric light curve of SN 2023fyq using a combination of shock breakout and CSM-interaction models. Bottom: Fits to the bolometric light curve of SN 2023fyq using a combination of shock breakout, CSM interaction, and ^{56}Ni decay models. The gap between 30 and 60 days in the ^{56}Ni decay model, indicated by the dashed line, is due to the transition from the photospheric phase to the nebular phase (see S. Valenti et al. 2008 for more details). The upper right panel is a zoom-in of the bottom panel to better illustrate the fit close to the SN peak. The initial bump is well fitted by the shock breakout model. The hollow point is at the precursor phase, so it is not included in the fit.

Fe and Co. However, as we discussed in Section 5, the nebular spectrum of SN 2023fyq is mainly dominated by He, O, and Ca. Therefore, we disfavor the ^{56}Ni decay as the dominant power source of the early light curve of SN 2023fyq.

6.2.2. CSM Interaction?

Since the evolution of SN 2023fyq is similar to those of Type Ibn SNe, it is likely that the light curve around the second peak is powered by CSM interaction. It is important to note that, since the spectra after the peak show signals from the SN ejecta but lack prominent narrow He lines, an asymmetric CSM structure must be involved if the second peak is dominated by CSM interaction.

We use the model presented in B. Jiang et al. (2020), which generalizes the self-similar solution to the interaction of stellar ejecta with surrounding CSM originally presented in R. A. Chevalier (1982). In this model, the density of CSM is described by a power law, $\rho \propto qr^{-s}$, while the ejecta are divided by an inner region ($\rho_{\rm ej} \propto r^{-\delta}$) and an outer region ($\rho_{\rm ej} \propto r^{-n}$). We fix the optical opacity (κ) to be 0.1 cm^2 g^{-1}, $n = 10$, $s = 0$, and $\delta = 1$ following C. Pellegrino et al. (2022). The value of $\kappa \approx 0.1$ cm^2 g^{-1} is motivated by the opacity of singly ionized He at $\sim 10^4$ K (e.g., I. K. W. Kleiser & D. Kasen 2014). We also attempted to fit the data with $s = 2$ (wind-like CSM), but did not achieve a reasonable fit. This result is consistent with the findings reported by E. Karamehmetoglu et al. (2017), A. Gangopadhyay et al. (2020), and T. Ben-Ami et al. (2023). The ejecta velocity (7000 km s^{-1}) is obtained from the velocity of the P-Cygni minimum of the He I lines near peak. The free parameters in our fit are the explosion epoch ($t_{\rm exp}$), the ejecta mass ($M_{\rm ej}$), the inner radius of the CSM (R_0), the CSM mass ($M_{\rm csm}$), the density of the CSM at R_0 ($\rho_{\rm csm,0}$), and the conversion efficiency of the shock kinetic energy to radiation (ϵ).

To account for the initial shock cooling phase, we have incorporated the SBO model presented by B. Margalit (2022). This model provides an analytic solution for the shock cooling phase following SBO from extended optically thick material, which is suitable for the case of SN 2023fyq. We fix the velocity of the inner envelope at 7000 km s^{-1}. Additionally, we introduce two free parameters into our fit: the radius of the extended material (R_e) and the mass of the extended material (M_e).

The model fit to the observed light curve is performed using an MCMC routine. As illustrated in the upper left panel of Figure 10, both the initial bump and the subsequent evolution of the light curve are well fitted by the model. The best-fitting parameters are detailed in Table 1 (CSM+SBO model). It is

Table 1

Best-fit Parameters of the CSM+Shock Breakout Model and the CSM+Shock Breakout+RAD Model

Model	$t_{\rm exp}$ (days)	$M_{\rm ej}$ ($M_\odot$)	R_0 (10^{13} cm)	$M_{\rm csm}$ ($M_\odot$)	$\rho_{\rm csm,0}$ (log 10(g cm $^{-3}$)	ϵ	R_e (10^{13} cm)	M_e ($M_\odot$)	$M_{\rm Ni}$ ($M_\odot$)
CSM+SBO	$-11.8^{+0.1}_{-0.1}$	$1.3^{+0.1}_{-0.1}$	$16.0^{+14.2}_{-9.7}$	$0.7^{+0.1}_{-0.1}$	$-11.9^{+0.1}_{-0.1}$	$5^{+0.1}_{-0.1}$ ´ 10^{-2}	$24.2^{+0.6}_{-1.1}$	$0.4^{+0.1}_{-0.1}$	…
CSM+SBO+RAD	$-11.7^{+0.1}_{-0.1}$	$1.2^{+0.1}_{-0.1}$	$15.0^{+12.5}_{-10.0}$	$0.6^{+0.1}_{-0.1}$	$-12.2^{+0.1}_{-0.1}$	$5^{+0.1}_{-0.1}$ ´ 10^{-2}	$21.4^{+0.7}_{-0.6}$	$0.3^{+0.1}_{-0.1}$	$0.02^{+0.01}_{-0.01}$

important to note that the models presented here are likely simplified, so the parameters derived can only be considered as estimations of the order of magnitude.

Shortly after the peak, the spectra of SN 2023fyq exhibit broad absorption lines from the SN ejecta, indicating an optically thin CSM-interaction region between the observer and the SN ejecta. However, the model fit indicates that the light curve is still predominantly influenced by the CSM interaction. One possible explanation for this discrepancy is that our analytical model is oversimplified, leading to an overestimation of the contribution from the CSM interaction. Alternatively, the CSM may not be spherically symmetric. For instance, if the SN were surrounded by a disk/torus-like CSM, strong CSM interaction would mainly occur in the equatorial region. Consequently, an observer looking along the polar direction would observe less obscured signals from the SN ejecta while the majority of the luminosity arises from the CSM interaction. In this case, the narrow lines from the equatorial CSM interaction would not be observed after the interaction region is enveloped by the expanding SN ejecta. The physical picture of this disk-like CSM scenario has been extensively discussed in N. Smith (2017).

The $M_{\rm ej}$ and $M_{\rm csm}$ derived for SN 2023fyq are roughly consistent with those found in other studies (e.g., C. Pellegrino et al. 2022; T. Ben-Ami et al. 2023). The low ejecta mass implies that the progenitor is likely a low-mass He star. However, this model can only fit the light curve around the peak and cannot explain the light-curve flattening at late times (see Figure 5). At later times, the light curve is likely powered by another source of energy.

6.2.3. RAD+CSM Interaction?

Since SN 2023fyq is similar to normal SESNe shortly after peak and during nebular phases, it is plausible that a certain amount of ^{56}Ni is produced during the explosion. Therefore, it is natural to consider ^{56}Ni decay as an additional energy source. A ^{56}Ni decay model has been employed to interpret the late-time light curves of many other Type Ibn SNe, often revealing low ^{56}Ni masses across previous studies (A. Gangopadhyay et al. 2020; C. Pellegrino et al. 2022; T. Ben-Ami et al. 2023).

We use the ^{56}Ni decay model presented in W. D. Arnett (1982) and S. Valenti et al. (2008). The full SN light curve is fitted by a combination of CSM interaction, SBO, and ^{56}Ni decay models. We fix the optical opacity to be $\kappa = 0.1$ cm^2 g^{-1} and the gamma-ray opacity to be 0.03 cm^2 g^{-1}. The ejecta velocity is fixed to be 7000 km s^{-1}. The best-fit model is shown in the upper right panel and the bottom panel of Figure 10, and the best-fit parameters are presented in Table 1 (the CSM+SBO+radioactive decay, hereafter RAD, model). Both the amount of ^{56}Ni ($\sim$0.02 $M_\odot$) and the ejecta mass ($\sim$1.2$M_\odot$) are lower than those of SESNe (J. D. Lyman et al. 2016). The low ejecta mass implies that the progenitor of SN 2023fyq is less massive than those of normal SESNe right before the SN explosion. One caveat of the model is that we did not consider the CSM interaction at late phases, which may affect the ^{56}Ni mass we derive here.

The parameters we derive here can give some insights about the progenitor of SN 2023yq. The radius of the extended material (R_e) is around 21×10^{13} cm ($\sim$3000 $R_\odot$). This large radius is consistent with the blackbody radius of SN 2023fyq around the SBO (Figure 5). This indicates that, at the explosion, the progenitor is surrounded by an extended envelope with a mass of 0.3 $M_\odot$ at a radius of $R_e \sim 3000 R_\odot$, consistent with what we discussed in Section 6.1. Considering the width of the narrow line component in the SN spectra (Figure 5) and the narrow lines observed pre-explosion (S. J. Brennan et al. 2024), the extended material likely expands with a velocity of $\sim$1000 km s^{-1}. Such a velocity suggests that the material at around $\sim$3000 $R_\odot$ was formed within around 20 days before the explosion.

In such a scenario, the pre-explosion photophere would be located within the extended material where the optical depth is sufficiently high. For a wind profile $\rho \propto r^{-2}$, $R_{BB} = \frac{kM}{4\,p\,tV_{\rm wind}}$ is roughly proportional to $M/V_{\rm wind}$, where M is the mass-loss rate, $V_{\rm wind}$ is the expansion velocity of the extended material, and τ is the optical depth at the photosphere. Consequently, the expansion of R_{BB}, starting from around -100 days (Figure 5), is likely due to an increase of mass loss. The more pronounced rise between ~ -40 and -11 days can be attributed to a more eruptive mass loss immediately preceding the explosion. If the majority of the material characterized by M_e is formed during this eruptive phase, the mass-loss rate can be estimated to be

$$M \text{ » } \frac{M_e V_{\rm wind}}{R_e} \text{ »} 4.5\, M \;\; \mathrm{yr}^{-1} \frac{M_e}{0.3M} \frac{3000R}{R_e} \frac{V_{\rm wind}}{1000\ \mathrm{km\ s}^{-1}}. \tag{1}$$

Interestingly, eruptive mass ejections on the order $\sim$0.1–1 $M_\odot$ are anticipated for low-mass He stars with masses of 2.5–3.2 $M_\odot$ due to core silicon deflagration or detonation weeks prior to core collapse (S. E. Woosley 2019; T. Ertl et al. 2020). The mass and velocity of the ejected material depend on the amount of silicon that is consumed in the burning process (T. Ertl et al. 2020). An ejection mass of $\sim$0.3 $M_\odot$ with a velocity of $\sim$1000 km s^{-1} is consistent with the typical values of such events (see Figure 14 and Table 4 of S. E. Woosley 2019).

The CSM characterized by $M_{\rm CSM}$ is likely more extended and formed during the earlier phase of the precursor activities. Detailed discussion on this topic is provided in Section 6.3.2.

In summary, neither RAD nor CSM interaction alone can be the power source of SN 2023fyq. Approximately a few weeks before the explosion, about 0.3 $M_\odot$ of material is ejected with a velocity of $\sim$1000 km s^{-1} due to an increase in mass loss from the progenitor. This material expands to a radius of $\sim$3000 $R_\odot$ at the time of the explosion. After the explosion, the energy deposited by the SBO from the extended material produces the initial light-curve bump. Around 0 day, the light curve is at least partially powered by the interaction between the SN ejecta and the surrounding CSM, with the kinetic energy of the ejecta converted into thermal energy, resulting in a bright peak. After that, as the strength of the CSM interaction decreases over time, the light curve becomes more influenced by RAD, leading to a relatively flat light curve.

6.3. What Powers the Precursor of SN 2023fyq?

6.3.1. Single Massive-star Activities?

SN precursors have been commonly observed in Type IIn SNe (e.g., N. Smith et al. 2010; A. Pastorello et al. 2013; E. O. Ofek et al. 2013; J. C. Mauerhan et al. 2013; E. O. Ofek et al. 2014; L. Tartaglia et al. 2016; A. Pastorello et al. 2018; N. L. Strotjohann et al. 2021; D. Hiramatsu et al. 2024), but are rarely found in Type Ibn SNe and Type II SNe. To date, the pre-explosion activities for Type Ibn SNe have only been detected in SN 2006jc (A. Pastorello et al. 2007) and SN 2019uo (N. L. Strotjohann et al. 2021). Searches for precursors in other SNe Ibn yielded only upper limits, ranging from around −15 to −13 mag (e.g., A. Pastorello et al. 2008a; I. Shivvers et al. 2017; Q. Wangq et al. 2024). This may be because those SNe Ibn had no precursors or only fainter and shorter ones, and also because most of these events occur at greater distances than SN 2023fyq. Compared to SN 2006jc and SN 2019uo, one unique characteristic of SN 2023fyq is the long-standing precursor emission. Precursor emission observed in SN 2006jc and SN 2019uo is around hundreds of days before the SN explosions with duration of ∼10 days. The precursor observed in these events are much shorter and brighter than that in SN 2023fyq (see Figure 2).

We first consider the possibility that the precursor of SN 2023fyq is produced by the final-stage stellar activities of a single massive star. In this case, the precursor can be powered by mass ejection driven by wave transport during the late-stage nuclear burning in the core (E. Quataert & J. Shiode 2012; J. H. Shiode & E. Quataert 2014; J. Fuller 2017; J. Fuller & S. Ro 2018; V. Morozova et al. 2020) or pulsational pair instability (T. Yoshida et al. 2016; S. E. Woosley 2017).

Massive stars with He core masses of 30–64 $M_\odot$ experience pulsational pair instability after carbon burning, producing violent mass ejections before their cores collapse (S. E. Woosley 2017). Pulsational pair instability in massive stars has been suggested to be a promising channel of Type Ibn SNe (T. Yoshida et al. 2016; S. E. Woosley 2017; S.-C. Leung et al. 2019; M. Renzo et al. 2020). The pulsing activities can last for hours to 10,000 yr, depending on the He core mass, before the SN explosion (T. Yoshida et al. 2016; S. E. Woosley 2017). In SN 2023fyq, precursor emission is detected for ∼3 yr before the SN explosion. Therefore, if pulsational pair instability powers the precursor emission of SN 2023fyq, the progenitor would be a He star with a zero-age main-sequence mass larger than ∼52 $M_\odot$ (S. E. Woosley 2017). However, the outbursts caused by the pulses of these more massive stars are usually energetic and can result in sharply rising light curves, which is inconsistent with the relatively steady precursor emission of SN 2023fyq. Additionally, the low ejecta mass we derived in Section 6.2 does not align with a very massive He star progenitor. Therefore, we disfavor pulsational pair instability as the powering mechanism of precursor emission in SN 2023fyq.

Strong temperature gradients can form during late-stage nuclear burning in massive stars, which generates convection, exciting internal gravity waves. The gravity waves may carry their energy to the envelope of the star and deposit it there (E. Quataert & J. Shiode 2012; J. H. Shiode & E. Quataert 2014; J. Fuller 2017; J. Fuller & S. Ro 2018), which may trigger eruptive mass ejections (S.-C. Leung & J. Fuller 2020; C. D. Matzner & S. Ro 2021). The mass ejection itself and the collision between the ejecta generated from multiple outbursts can potentially produce SN precursor emission (S.-C. Leung & J. Fuller 2020; N. L. Strotjohann et al. 2021; D. Tsuna et al. 2023). However, it would be difficult to reproduce the timescale of the observed precursor with a single event of dynamical envelope ejection from a stripped star (D. Tsuna et al. 2024a). This is because the timescale is regulated by radiative diffusion from the precursor ejecta, which is only weeks to months for stripped stars; thus, it would work for the precursors of SN 2006jc or SN 2019uo (D. Tsuna et al. 2024a), but not for SN 2023fyq. In order to produce the precursor emission seen in SN 2023fyq, multiple fine-tuned mass ejections would be needed. Therefore, a more plausible scenario is a continuous mass loss over the timescale of years, with some continuous powering mechanism for the precursor.

6.3.2. Binary Interaction?

A low-mass He star in a binary system has been proposed to be a possible progenitor scenario for Type Ibn SNe (J. R. Maund et al. 2016; L. Dessart et al. 2022; D. Tsuna et al. 2024a), which is supported by the lack of star formation at the site of some members of the class (N. E. Sanders et al. 2013; G. Hosseinzadeh et al. 2019). In this section, we explore the possibility that the progenitor of SN 2023fyq is an exploded stripped star, such as a He star, in a binary system and that the binary mass transfer generated the precursor activities.

The stripped SN progenitor in a binary system expands at some point in its evolution near core collapse, filling its Roche lobe and initiating mass transfer onto the companion. Such a scenario is expected for stripped stars with He core masses in the range of 2.5–3 $M_\odot$, which can inflate their envelopes to up to ∼100 $R_\odot$ at the oxygen/neon burning phase in the final years to decades of their lives (e.g., S. C. Wu & J. Fuller 2022, and references therein). Thus, for orbital separations of ∼(1–few) ×100 $R_\odot$ (orbital period of order 100 days for a companion of order ∼1$M_\odot$), we expect intense mass transfer to initiate during this time period.

If the accretor is a compact object, the mass-transfer rate is typically orders of magnitude higher than its Eddington rate, $M_{\rm Edd} \sim 2 \times 10^{-8}\, M_\odot\, {\rm yr}^{-1} (M_{\rm comp}/1M_\odot)(\kappa_{\rm opt}/0.1\ {\rm cm}^2\ {\rm g}^{-1})^{-1}$ (where a radiation efficiency of 10% was assumed), and thus, most of the transferred mass actually escapes from the binary system without being accreted onto the compact object. Even if the companion is not a compact object, for large mass-transfer rates of $\gtrsim 10^{-4}$–$10^{-3}\, M_\odot\, {\rm yr}^{-1}$, most of the mass is expected to still escape through the binary's outer Lagrange point (W. Lu et al. 2023). In either case, this escaped material becomes the CSM that later powers the bright SN.

In Section 6.2, we found that the CSM required to power the main SN light curve is around $0.6^{+0.1}_{-0.1}\, M_\odot$, which requires a time-averaged mass-loss rate of around a few $0.1 M_\odot\, {\rm yr}^{-1}$ given that the mass loss is linked to the observed 1000 day precursor.

For binary systems exhibiting such high mass-loss rates suggested by S. C. Wu & J. Fuller (2022), those with orbital periods ranging from 10 to 100 days are favored. These systems have orbital velocities of $\sim$100—a few 100 km s^{-1}. Assuming the velocity of the CSM that escapes the binary system is $\sim$200 km s^{-1}, the mass-loss rate via mass transfer should be at least larger than $\sim 2\times10^{-2}\,M_\odot\,\mathrm{yr}^{-1}$ to power the light-curve peak (the detailed derivation is shown in Appendix B), which is consistent with what we found in Section 6.2.

Given the required $\dot{M}$, we can consider two mechanisms to power the precursor emission. The first is a collision of the mass-transfer outflow with external material, which may exist due to a previous mass-transfer episode (e.g., O. Pejcha et al. 2016; B. D. Metzger & O. Pejcha 2017). While we remain agnostic to the origin of the preexisting matter, the maximum available power is given by the kinetic luminosity of the outflow as

$$L_{\rm out} \approx \frac{1}{2}\dot{M}v_{\rm CSM}^2 \simeq 1.3\times10^{39}\ {\rm erg\ s^{-1}} \times \left(\frac{\dot{M}}{0.1M_\odot\ {\rm yr^{-1}}}\right)\left(\frac{v_{\rm CSM}}{200\ {\rm km\ s^{-1}}}\right)^2. \tag{2}$$

Thus, the precursor may be explained, but only for favorably high CSM velocity as well as high efficiencies for dissipation and radiation conversion close to unity.

In the case for a compact object companion, an accretion disk forming around the compact object can be a promising energy source. While most of the transferred mass is removed from the outer L2 point, a small fraction can still accrete onto the companion and form a disk. The disk, if its accretion rate is super-Eddington, can launch a fast radiation-driven wind that can collide with the rest of the mass and dissipate its kinetic energy.

The hydrodynamics of the transferred mass has been considered recently in W. Lu et al. (2023). For a neutron star companion with an orbital separation of $a\approx$ (1–few) $\times$ 100 $R_\odot$ and mass-transfer rate $\gg10^{-3}\,M_\odot\,\mathrm{yr}^{-1}$, most of the mass is indeed lost from the L2 point (their $f_{\rm L2}\sim1$). However, the accretion rate can still reach $\dot{M}_{\rm acc}\sim(3\text{–}7)\times10^{-4}\,M_\odot\,\mathrm{yr}^{-1}$ (Figure A2 of W. Lu et al. 2023), which is orders of magnitude larger than the Eddington rate.

For a binary mass ratio of $q=M_{\rm NS}/M_*\approx0.5$, the (Keplerian) circularization radius of the disk is found from the fitting formula in W. Lu et al. (2023) as

$$R_c \approx 0.10a \simeq 7\times10^{11}\ {\rm cm}\left(\frac{a}{100R_\odot}\right). \tag{3}$$

We expect a disk wind to be launched roughly where the local luminosity exceeds the Eddington luminosity of the neutron star (NS), within a disk radius (Equation (31) of W. Lu et al. 2023)

$$R_{\rm sph} \approx \frac{\dot{M}_{\rm acc}\kappa}{4\pi c} \simeq 2\times10^{10}\ {\rm cm}\left(\frac{\dot{M}_{\rm acc}}{5\times10^{-4}M_\odot\ {\rm yr^{-1}}}\right)\left(\frac{\kappa}{0.2\ {\rm cm^2\ g^{-1}}}\right), \tag{4}$$

which is typically less than $R_{\rm c}$ for an orbital separation of $a\sim100\,R_\odot$. We have taken the opacity here to be $\kappa\approx0.2\ \mathrm{cm^2\ g^{-1}}$ as helium is expected to be fully ionized in the interior of the disk. In line with many theoretical works that model super-Eddington disk winds, we assume a power-law accretion rate $\dot{M}$ of $\dot{M}\propto r^p$ ($R_{\rm NS}<r<R_{\rm sph}$), where we adopt $R_{\rm NS}=10$ km. This means that a fraction of the accreted mass is expelled at each radius, and we assume that the wind velocity is equivalent to the local disk escape velocity. Consequently, the wind kinetic luminosity, integrated over the range of r, is estimated as

$$L_{\rm wind} \approx \frac{p}{2(1-p)}\dot{M}_{\rm acc}\frac{GM_{\rm NS}}{R_{\rm NS}}\left(\frac{R_{\rm NS}}{R_{\rm sph}}\right)^p \simeq 2\times10^{40}\ {\rm erg\ s^{-1}}\left(\frac{\dot{M}_{\rm acc}}{5\times10^{-4}M_\odot\ {\rm yr^{-1}}}\right)^{1/2} \times\left(\frac{M_{\rm NS}}{1.4M_\odot}\right)\left(\frac{\kappa}{0.2\ {\rm cm^2\ g^{-1}}}\right)^{-1/2} \tag{5}$$

where we have adopted $p=0.5$ in the last equation while a possible range of $0.3\leqslant p\leqslant0.8$ is suggested (F. Yuan & R. Narayan 2014). We thus find that the disk wind carries the appropriate kinetic luminosity to explain the precursor in the steady-state phase.

As the disk wind carries much smaller mass than the rest of the material around the system, its kinetic energy will be efficiently dissipated by their collision. We check that the dissipated energy would be successfully radiated as the precursor. For a wind profile, the diffusion timescale in the CSM is

$$t_{\rm diff} \approx \frac{\kappa\dot{M}}{4\pi v_{\rm CSM}c} \simeq 8\times10^4\ {\rm sec}\left(\frac{\dot{M}}{0.1M_\odot\ {\rm yr^{-1}}}\right)\left(\frac{\kappa}{0.1\ {\rm cm^2\ g^{-1}}}\right)\left(\frac{v_{\rm CSM}}{200\ {\rm km\ s^{-1}}}\right)^{-1}, \tag{6}$$

and the adiabatic expansion timescale from the dissipation region, whose size is roughly comparable to the orbital separation, is

$$t_{\rm exp} \approx \frac{a}{v_{\rm CSM}} \simeq 3\times10^5\ {\rm sec}\left(\frac{a}{100\ R_\odot}\right)\left(\frac{v_{\rm CSM}}{200\ {\rm km\ s^{-1}}}\right)^{-1}. \tag{7}$$

Thus, we expect that the dissipated energy can be successfully radiated away without adiabatic losses. The radiation will be reprocessed in the CSM, and finally be emitted as optical radiation at $r\approx R_{\rm BB}$. We refer to D. Tsuna et al. (2024b) for detailed light-curve modeling at the precursor phase.

The mass loss via the L2 point can form an equatorial disk (e.g., W. Lu et al. 2023). The interaction of the equatorial disk with the SN ejecta may contribute to the second peak of the SN light curve. In this case, the parameter $M_{\rm CSM}$ mentioned in Section 6.2 roughly characterizes the mass of the equatorial disk. The interaction of SN ejecta with this dense CSM may still continue in the nebular phase, producing the intermediate-width He lines we observe.

In this binary scenario, an accretion disk might form inside the ejecta after the SN explosion. The outflow from the disk may dissipate its kinetic energy through collisions with previously ejected matter, potentially becoming an additional power source for the SN light curve. In this case, the amount of CSM derived in Sections 6.2.2 and 6.2.3 might be overestimated.

6.3.3. What About the Rise after −100 Days in the Pre-explosion Light Curve?

As we mentioned in Section 4.3, the pre-explosion light curve shows a rapid rise after −100 days, with a more pronounced rise occurring between −40 and −11 days. This may be associated with eruptive mass loss right before the SN explosion. For the more pronounced rise between −40 and −11 days, we consider two possibilities: (1) The rise is due to orbital shrinking of the binary, leading to a runaway of mass transfer and resulting in a rapid-rising pre-explosion light curve (i.e., M. MacLeod et al. 2018). (2) The rise is influenced by the core silicon burning of the He star, which ejects a large amount of material and powers the fast-rising light curve just before the core collapses.

For the first case, we initially consider the orbital evolution of this binary system over the few-year timescale during which we observe the precursor. The mass loss from the Lagrange point carries away angular momentum as well, which can affect the orbital separation of the binary. This generally leads to shrinking of the orbit, which may have been witnessed as the sharp rise of the light curve as we approach the explosion epoch. From Figure 5 of W. Lu et al. (2023), we find the orbital shrinking rate for mass ratio $q = 0.5$ and $f_{\mathrm{L2}} = 1$ as

$$\frac{\dot{a}}{a} \approx (q-5)\frac{\dot{M}}{M_*} \sim -(6\ \mathrm{yr})^{-1}\left(\frac{\dot{M}}{0.1M_\odot\ \mathrm{yr}^{-1}}\right)\left(\frac{M_*}{3M_\odot}\right)^{-1}, \quad (8)$$

which means that for a mass-loss rate of $\sim 0.1 M_\odot\ \mathrm{yr}^{-1}$; the orbital separation can significantly shrink in the several years that we observe the precursor. The orbital shrinking of the binary may cause an unstable mass transfer and accretion onto the compact object, resulting in a runaway mass loss. This may explain the rapid rise after around −40 days in the precursor light curve. Given the anticipated significant orbital shrinking within several years for the system under consideration, the shallower rise in the light curve between −100 and ∼ −40 days is likely also influenced by the orbital shrinking. This may only lead to a gentle increase in the accretion rate onto the compact companion, resulting in the rise of the light curve.

In this scenario, the final SN explosion can be due to the merger of the He star with a compact object (e.g., R. A. Chevalier 2012; N. Soker 2019; B. D. Metzger 2022). Such merger-driven explosions have been proposed to explain some long gamma-ray bursts (C. L. Fryer & S. E. Woosley 1998; W. Zhang & C. L. Fryer 2001; C. C. Thöne et al. 2011; C. L. Fryer et al. 2013), which are usually associated with a subtype of Type Ic SNe that exhibit broad spectral lines. This He-merger scenario can connect the observed rapid increase in the light curve's brightness at the end of the precursor phase with the following SN-like explosion. However, the characteristics of the final explosion postmerger remain poorly understood. For example, the predicted explosion energies are uncertain by many orders of magnitude (C. L. Fryer & S. E. Woosley 1998; W. Zhang & C. L. Fryer 2001; S. L. Schrøder et al. 2020). While the merger-driven explosion might explain the spectral features observed, detailed spectral modeling of these events is still lacking.

For the second case, a core-collapse SN explosion is anticipated after significant mass transfer over years from low-mass stripped stars ranging from 2.5 to $3 M_\odot$ (S. C. Wu & J. Fuller 2022). Additionally, an explosive mass ejection weeks before the explosion due to silicon burning is indeed expected in recent studies for low-mass He stars with masses of 2.5–3.2 $M_\odot$ (S. E. Woosley 2019). The mass ejected can range from 10^{-2} to 1 $M_\odot$ with velocities from $\sim 100\ \mathrm{km\ s^{-1}}$ to a few $1000\ \mathrm{km\ s^{-1}}$. In Section 6.2, we found that there is likely an eruptive mass loss of $\sim 0.3\,M_\odot$ a few weeks before the SN explosion with a velocity of $\sim 1000\ \mathrm{km\ s^{-1}}$, which is consistent with the silicon burning phase for low-mass He stars. The eruptive mass loss may explain the more pronounced rise of the precursor light curve between ∼ −40 and −11 days, and the ejected material in turn produces the first SN peak. However, we note that detailed light-curve modeling is necessary to confirm this hypothesis. In this case, the shallower rise in the light curve between −100 and ∼ −40 days is likely still attributed to the orbital shirking of the binary system, like discussed above.

In this scenario, the final SN explosion results from the core collapse of the He star. This explanation accounts for the observed spectral similarities between SN 2023fyq and SESNe both postpeak and during the nebular phases.

Both the merger-driven and core-collapse scenarios can account for certain observed features of SN 2023fyq. In either case, the progenitor system would likely be asymmetric, which aligns with observations of SN 2023fyq. The ^{56}Ni yields from a merger-driven explosion are likely low (C. L. Fryer et al. 2013; B. D. Metzger 2022), and, similarly, low ^{56}Ni production is expected from core-collapse explosions in low-mass helium stars (S. E. Woosley 2019). These predictions are consistent with the low ^{56}Ni mass derived from the late-time light curves of SN 2023fyq.

An important difference between these two scenarios is that a merger-driven explosion typically results in a single compact object in the remnant, whereas a core-collapse explosion generally leaves behind a compact binary. In the core-collapse scenario, fallback accretion postexplosion could produce observable X-ray emissions approximately 100–1000 days after the explosion, which may show time variations tied to the orbital motion of the binary (K. Kashiyama et al. 2022). This kind of time variations will not be observed in the merger-driven scenario since there will be only a single compact object left. For SN 2023fyq, conducting X-ray follow-up years after the explosion could be helpful in distinguishing between these two scenarios in future studies.

We expect X-ray emission when it is transparent to photoionization by oxygen and carbon in the ejecta. Our modeling favors low-mass (a few $M_\odot$) helium stars for the progenitor, with carbon-oxygen cores of mass ≈1.5–2 $M_\odot$. For an explosion ejecta from such progenitors, we infer the mass of carbon/oxygen-rich material to be roughly $M_{\mathrm{ej,\,C/O}} \sim 0.1$–$1\,M_\odot$. The lower limit applies if a neutron star is left behind in the explosion (as in ultrastripped SNe considered in K. Kashiyama et al. 2022), and the upper limit is if the bulk of the CO-core is disrupted (e.g., by a merger) and becomes part of the SN ejecta. Adopting the ejecta velocity of $v_{\mathrm{ej}} = 7000\ \mathrm{km\ s^{-1}}$ and the X-ray photoionization cross section of $\sigma_{\mathrm{X}} \sim 10^{-19}\ \mathrm{cm^2}(h\nu/\mathrm{keV})^{-3}$, we expect X-rays with energy $h\nu$ to be transparent at

$$t_{\mathrm{trans}} \sim \sqrt{\frac{\sigma_{\mathrm{X}} M_{\mathrm{ej,C/O}}/14 m_p}{4\pi v_{\mathrm{ej}}^2}} \sim 1\ \mathrm{yr}\left(\frac{M_{\mathrm{ej,\,C/O}}}{0.1\,M_\odot}\right)^{1/2}\left(\frac{h\nu}{5\ \mathrm{keV}}\right)^{-3/2}. \quad (9)$$

Thus, follow-up in hard X-rays at years after the explosion is encouraged, although the X-ray luminosity would depend on the uncertain degree of fallback ($\sim 10^{39}$–10^{40} erg s^{-1} at peak, K. Kashiyama et al. 2022). If the fallback is similar to the ultrastripped SN models in K. Kashiyama et al. (2022), we expect the source to be detectable by current X-ray facilities thanks to the proximity of this event.

In conclusion, the timescale and brightness of the precursor observed in SN 2023fyq before −100 days can be attributed to mass transfer in a binary system. The companion star is likely a compact object, as the energetics of the disk wind launched from super-Eddington accretion onto the compact object can naturally explain the luminosity of the precursor. An equatorial circumbinary disk, formed during the mass transfer, later interacts with the SN ejecta, powering the main SN peak. During the nebular phases, the ongoing interaction between the equatorial disk and the SN ejecta produces the intermediate-width He lines observed. The rise of the light curve between −100 and ∼ −40 days is likely due to orbital shrinking. The more pronounced rise of the light curve starting around −40 days may be linked to (1) an eruptive mass ejection due to final-stage silicon burning, or (2) runaway mass transfer caused by orbital shrinking of the binary system. In the first scenario, the subsequent explosion would result from the core collapse of the He star. In the second scenario, it would result from the merger of the He star with the compact object. Both scenarios can launch materials into the polar region. The SBO from this extended material and the following cooling emission power the first bright SN peak.

6.4. Connections to Other Transient Phenomena and Implications on the CSM Structure

It is noteworthy that the light-curve morphology (both the pre- and postexplosion phase) of SN 2023fyq is quite similar to those of luminous red novae (N. Soker & R. Tylenda 2003; R. Tylenda et al. 2011; J. C. Mauerhan et al. 2015; N. Smith et al. 2016; N. Blagorodnova et al. 2017), which are generally understood to be the product of binary mergers (e.g., B. D. Metzger & O. Pejcha 2017; N. Soker 2024). The pre-explosion activities in luminous red novae are often associated with binary mass transfer (e.g., O. Pejcha 2014), and the pre-explosion brightening is due to the increase in the mass-loss rate caused by orbital shrinking. The postexplosion light curves of luminous red novae are double peaked, in which the first peak is likely from the shock cooling, and the second peak is from the interaction between the ejecta and a preexisting equatorial disk formed during binary mass transfer (B. D. Metzger & O. Pejcha 2017).

The scenario for luminous red novae is analogous to what we proposed for SN 2023fyq, and the primary difference is just the explosion energy source. Such an asymmetric CSM structure is consistent with the multicomponent profile of the He I λ5876 line as we discussed in Section 5 and also the asymmetric line profiles observed during the pre-explosion phase of SN 2023fyq (S. J. Brennan et al. 2024). Similarities between luminous red novae and interaction-powered SNe have also been reported in previous studies (e.g., D. Hiramatsu et al. 2024).

The SN light-curve evolution of SN 2023fyq is similar to those of ultrastripped SNe (K. De et al. 2018; Y. Yao et al. 2020). The first bright SN light-curve peak in these ultrastripped SNe is generally understood as a result of SBO from the dense CSM ejected weeks before the SN explosion. The second peak of these objects is usually around 10^{42} erg s^{-1}, much fainter than that of SN 2023fyq, and is thought to be powered by ^{56}Ni decay (K. De et al. 2018; Y. Yao et al. 2020). It may be that in these objects the CSM is more confined, and a more extended ($\sim 10^{15}$ cm) dense equatorial disk is lacking, resulting in insufficient CSM at these radii to power the second peak through interaction like that observed in SN 2023fyq.

SN 2022jli has been proposed to be an SESN that exploded in a binary system (T. Moore et al. 2023; P. Chen et al. 2024). However, since the light curve and spectral evolution of SN2022jli are quite different from those of SN 2023fyq, these two events likely originated from different progenitor systems.

SNe Ibn can show a wide variety of spectral features at early phases (G. Hosseinzadeh et al. 2017), which is not surprising if all SNe Ibn experience strong interaction with asymmetric CSM (e.g., N. Smith et al. 2015; N. Smith 2017). Only a few SNe Ibn are observed until late phases since they can decline fast. Interestingly, as we show in Figure 9, at late times, these SNe Ibn seem to fall into two distinct classes: Class I that shows broad lines and shares many similarities with normal SESNe (SN 2023fyq, SN 2015G, SN 2018gjx) and Class II that is still dominated by narrow emission lines (SN 2006jc, SN 2019kbj). Assuming the progenitors of all these SNe Ibn are He stars, the objects in Class II may be surrounded by more massive CSM and/or have lower explosion energy (L. Dessart et al. 2022).

For the objects in Class I, the intensity of the [O I] $\lambda\lambda$ 6300, 6364 line can vary significantly among different objects while the other spectral features are quite similar. If the progenitors of all these objects are surrounded by an equatorial disk, the difference in the intensity of the [O I] $\lambda\lambda$ 6300, 6364 line can be naturally explained by different viewing angles (see Figure 11). If the system is observed from the equatorial direction, the central [O I] $\lambda\lambda$ 6300, 6364 line forming region can be obscured by the disk. Instead, a polar observer would be able to see the whole nebular emission from the inner ejecta. For both observers, intermediate-width He emission lines from the ongoing interaction of the SN ejecta with the equatorial disk can be seen.

A disk/torus-like CSM is also invoked in previous studies to explain the spectroscopic evolution of SNe Ibn (S. J. Prentice et al. 2020) and SNe IIn (e.g., N. Smith & J. E. Andrews 2020; N. Smith et al. 2015; J. E. Andrews & N. Smith 2018; N. Smith & J. E. Andrews 2020). Such a disk/torus-like CSM scenario could potentially explain the diversity we see in SNe Ibn in Class I, and is consistent with the precursor model we discussed in Section 6.3.2. This suggests that Class I SNe Ibn may originate from a similar progenitor channel but with variations in viewing angles.

Long-lasting and relatively stable precursor activities due to binary interaction are commonly seen in luminous red novae (e.g., R. Tylenda et al. 2011; J. C. Mauerhan et al. 2015; N. Blagorodnova et al. 2017). Given the similarity of the progenitor scenario of luminous red novae and SN 2023fyq, it is possible that precursor activities are not rare in SNe Ibn in Class I. If this is true, the long-lasting and slowly rising pre-explosion emission may serve as a unique early warning for this subclass of Type Ibn SNe. The evolution of the precursor light curves may vary depending on the viewing angle, as the

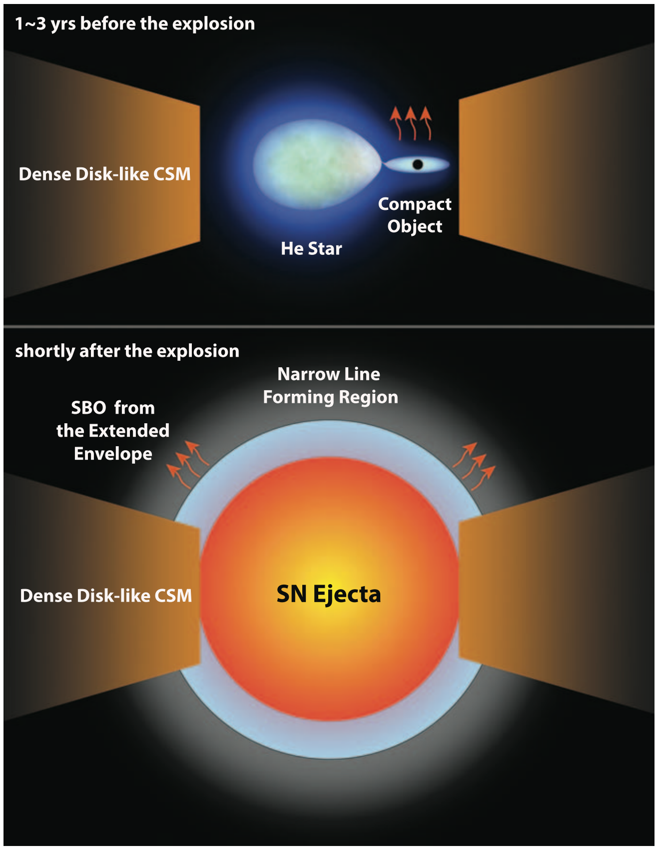

Figure 11. A sketch of the possible progenitor system of SN 2023fyq. Upper: around a few years before the explosion, the progenitor (a He star with a mass of $\sim$2.5–3 $M_\odot$) expands at the oxygen/neon burning phase, filling its Roche lobe. This triggers mass transfer onto its companion compact object, resulting in the precursor emission we observe. Around weeks before the explosion, an eruptive mass ejection is triggered through core silicon burning in the low-mass He star or runaway mass transfer due to orbital shrinking, launching dense material to the polar region. The subsequent explosion is likely due to either by core collapse of the He star or by the merger of the He star with its compact object companion. Bottom: Immediately after the explosion, the shock breaks out from the dense polar material formed weeks before the explosion, producing the first light-curve peak. The interaction of SN ejecta with the equatorial disk formed by the pre-explosion binary interaction contributes to the second peak.

emission could be obscured by the equatorial disk for observers near the equatorial plane. Given that the viewing angle also influences the intensity of the [O I] lines in the nebular spectra, combining the precursor emission with late-time spectroscopy could serve as a unique probe for the progenitor scenario we propose.

7. Summary

The evolution of SN 2023fyq closely resembles that of Type Ibn SNe. The optical spectra postpeak and the nebular spectrum of SN 2023fyq share similarities with those of normal SESNe, implying that the progenitor is a stripped/He star. The SN light curve can be reproduced by a CSM-interaction + SBO + ^{56}Ni decay model, implying the presence of dense CSM around the progenitor, a low progenitor mass, and a low ^{56}Ni production. The precursor emission of SN 2023fyq is observed up to around 3 yr before the SN explosion, which is best explained by the mass transfer in a binary system involving a low-mass He star.

Putting all these together, we summarize a possible timeline for SN 2023fyq:

1. *$\sim$−1000 to $\sim$−100 days (upper panel of Figure 11).* A low-mass He star (2.5–3 $M_\odot$) expands substantially at the oxygen/neon burning phase, triggering mass transfer to its companion compact object, which produces the precursor emission we observe. The outflow via L2 point produces the He-rich CSM around the progenitor system and forms an equatorial disk ($\sim$0.6$M_\odot$).
2. *$\sim$−100 to $\sim$−11 days.* The shrinkage of the orbit leads to an increase in the accretion rate onto the companion compact object, resulting in a rise in the light curve. The more pronounced light-curve rise after $\sim$ −40 days is likely due to either the core silicon burning or the runaway mass transfer caused by orbital shrinking, which triggers an eruptive mass ejection ($\sim$0.3$M_\odot$) with a velocity of $\sim$1000 km s^{-1}. This launches dense material to the polar region.
3. *$\sim$−11 days (bottom panel of Figure 11).* An SN explosion is triggered either by the core collapse of the He star or by the merger of the He star with a compact object, which sends a shock through the polar material ($\sim$3000 $R_\odot$). The energy deposited during the SBO produces the initial bump of the light curve.
4. *$\sim$−11 to $\sim$20 days.* The SN ejecta collide with the equatorial He-rich CSM ($\sim$0.6$M_\odot$), converting the kinetic energy of the SN ejecta into thermal energy, contributing to the SN light curve and generating a very blue spectrum with only prominent He lines. With the expansion of the ejecta, the optical depth decreases so that more signals from the SN ejecta are observed.
5. *After $\sim$20 days.* The strength of the CSM interaction decreases, and the SN fades, and RAD likely starts to contribute more to the light curve. Later, the ejecta become more optically thin, and the object transitions into the nebular phase. Given our proximity to the polar direction of the system, signals from the inner part of the ejecta are revealed, which closely resemble those of normal SESNe at nebular phases. Additionally, the continuing interaction between the ejecta and the He-rich equatorial CSM produces strong intermediate-width He emission lines.

Given the similarities between SN 2023fyq and other Type Ibn SNe, precursor activities may be common for a certain subclass of Type Ibn SNe. If an equatorial disk is indeed formed during the precursor phase, the precursor emission and the intensity of the [O I] lines at the nebular phases for this class of objects would be dependent on the viewing angle. It is worth noting that this mechanism does not apply to the very brief, singular pre-explosion outburst observed in SN 2006jc and SN 2019uo. For the upcoming LSST survey, a single 30 s visit will achieve a 5σ depth of approximately 24 mag (F. B. Bianco et al. 2022). By stacking images, even deeper limits can be achieved. This enables LSST to effectively constrain the precursors of Type Ibn SNe, such as SN 2023fyq, within 150 Mpc, assuming a typical precursor brightness of −12 mag. A sample of Type Ibn SNe with well-constrained precursor activities, combined with the late-time spectroscopy, will test the progenitor scenario we propose. We encourage X-ray follow-up on SN 2023fyq in the years following the explosion, as this will help distinguish between a merger-driven explosion and a core-collapse explosion as the mechanism for this event. We also encourage detailed spectral and light-curve modeling of merger-driven explosions, as well as the silicon burning phase in low-mass He stars just prior to core collapse. By comparing these models with a large sample of observations, we can deepen our understanding of the final stages of stellar evolution.

Acknowledgments

We would like to thank Jim Fuller for the assistance with the manuscript in its early stages. We would like to thank Kyle Davis for sharing the SOAR spectrum from the program. Y.D. would like to thank L.Z. for redesigning and redrawing Figure 11 in the paper.

Research by Y.D., S.V., N.M.R, E.H., and D.M. is supported by NSF grant AST-2008108. D.T. is supported by the Sherman Fairchild Postdoctoral Fellowship at the California Institute of Technology.

Time-domain research by the University of Arizona team and D.J.S. is supported by NSF grants AST-1821987, 1813466, 1908972, 2108032, and 2308181, and by the Heising-Simons Foundation under grant No. 2020-1864.

This work makes use of data from the Las Cumbres Observatory global telescope network. The LCO group is supported by NSF grants AST-1911225 and AST-1911151.

A.Z.B. acknowledges support from the European Research Council (ERC) under the European Union’s Horizon 2020 research and innovation program (grant agreement No. 772086).

This publication was made possible through the support of an LSST-DA Catalyst Fellowship to K.A.B, funded through grant 62192 from the John Templeton Foundation to LSST Discovery Alliance. The opinions expressed in this publication are those of the authors and do not necessarily reflect the views of LSST-DA or the John Templeton Foundation.

This work is based on observations obtained at the international Gemini Observatory, a program of NSF’s NOIRLab, which is managed by the Association of Universities for Research in Astronomy (AURA) under a cooperative agreement with the National Science Foundation; on behalf of the Gemini Observatory partnership: the National Science Foundation (United States), National Research Council (Canada), Agencia Nacional de Investigación y Desarrollo (Chile), Ministerio de Ciencia, Tecnología e Innovación (Argentina), Ministério da Ciência, Tecnologia, Inovações e Comunicações (Brazil), and Korea Astronomy and Space Science Institute (Republic of Korea).

This work was enabled by observations made from the Gemini North telescope, located within the Maunakea Science Reserve and adjacent to the summit of Maunakea. We are grateful for the privilege of observing the Universe from a place that is unique in both its astronomical quality and its cultural significance.

This work includes observations obtained at the Southern Astrophysical Research (SOAR) telescope, which is a joint project of the Ministério da Ciência, Tecnologia e Inovações (MCTI/LNA) do Brasil, the US National Science Foundation’s NOIRLab, the University of North Carolina at Chapel Hill (UNC), and Michigan State University (MSU).

Some of the data presented herein were obtained at Keck Observatory, which is a private 501(c)3 nonprofit organization operated as a scientific partnership among the California Institute of Technology, the University of California, and the National Aeronautics and Space Administration. The Observatory was made possible by the generous financial support of the W. M. Keck Foundation. The authors wish to recognize and acknowledge the very significant cultural role and reverence that the summit of Maunakea has always had within the indigenous Hawaiian community. We are most fortunate to have the opportunity to conduct observations from this mountain.

The LBT is an international collaboration among institutions in the United States, Italy, and Germany. LBT Corporation Members are The University of Arizona on behalf of the Arizona Board of Regents; Istituto Nazionale di Astrofisica, Italy; LBT Beteiligungsgesellschaft, Germany, representing the Max-Planck Society, The Leibniz Institute for Astrophysics Potsdam, and Heidelberg University; The Ohio State University, and The Research Corporation, on behalf of The University of Notre Dame, University of Minnesota, and University of Virginia.

This research has made use of the NASA/IPAC Extragalactic Database (NED), which is funded by the National Aeronautics and Space Administration and operated by the California Institute of Technology.

This research made use of Photutils, an Astropy package for detection and photometry of astronomical sources (L. Bradley et al. 2022).

Facility: ADS, DLT40 (Prompt5, Prompt-MO), ATLAS, LCOGT (SBIG, Sinistro, FLOYDS), Gemini:North (GMOS), Keck:I (LRIS, DEIMOS), NED, SOAR (Goodman), Swift (UVOT), LBT (MODS).

Software: Astropy (Astropy Collaboration et al. 2013, 2018, 2022), emcee (D. Foreman-Mackey et al. 2013), HOTPANTS (A. Becker 2015), Matplotlib (J. D. Hunter 2007), NumPy (C. R. Harris et al. 2020), PYRAF (Science Software Branch at STScI 2012), Pandas (W. McKinney 2010), SciPy (P. Virtanen et al. 2020), SWarp (E. Bertin et al. 2002), LCOGTSNpipe (S. Valenti et al. 2016), Light Curve Fitting (G. Hosseinzadeh & S. Gomez 2020), LPipe (D. A. Perley 2019).

Appendix A
Color Evolution

We present the $g-r$, $B-V$, and B_s-V_s color evolution of SN 2023fyq around its peak in Figure 12. Photometry data from both this work and S. J. Brennan et al. (2024) are used.

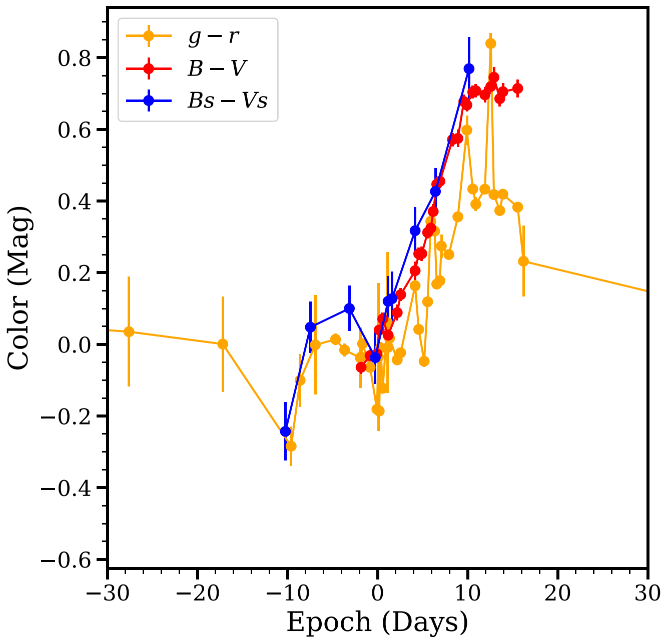

Figure 12. The evolution of $g-r$, $B-V$, and B_s-V_s colors. There is plateau phase in the color evolution between around −5 and 0 days, which is consistent with the temperature plateau shown in Figure 5.

Appendix B
The Mass-loss Rate in Binary Interaction Scenario

This appendix calculates the mass-loss rate needed for a binary system to explain the observations, as discussed in Section 6.3.2. We begin with estimating the required mass-loss rate $\dot{M}$ of the CSM, which in our scenario is equivalent to the mass-transfer rate if the rate is much larger than the Eddington rate, and the companion cannot accrete most of the transferred material. The CSM must be optically thick within the observed blackbody radius $R_{\rm BB}\approx 600\,R_\odot$ at the precursor phase. For a mass-loss rate of $\dot{M}$, the optical depth at $R_{\rm BB}$ is

$$\tau_{\rm CSM}(r=R_{\rm BB}) \approx \frac{\kappa\dot{M}}{4\pi R_{\rm BB}v_{\rm CSM}} \sim 60\left(\frac{\dot{M}}{0.1\,M_\odot\,{\rm yr}^{-1}}\right)\left(\frac{\kappa}{0.1\,{\rm cm}^2\,{\rm g}^{-1}}\right) \times\left(\frac{v_{\rm CSM}}{200\,{\rm km\,s}^{-1}}\right)^{-1} \quad ({\rm B1})$$

where $v_{\rm CSM}$ is the velocity of the CSM that escapes the binary system. This is typically the orbital velocity for outflows from mass transfer, which is ∼200 km s^{-1} for the orbital separation of interest (see Section 6.3.2), but the arguments below would not depend much on the adopted value. The value of $\kappa\approx 0.1\,{\rm cm}^2\,{\rm g}^{-1}$ is motivated from that of singly ionized helium at around 10^4 K (e.g., I. K. W. Kleiser & D. Kasen 2014). The optical depth then poses a lower limit in $\dot{M}$ of

$$\dot{M} \gtrsim \dot{M}_{\rm min} \approx 2\times 10^{-3} M_\odot\,{\rm yr}^{-1}\left(\frac{\kappa}{0.1\,{\rm cm}^2\,{\rm g}^{-1}}\right)^{-1} \times\left(\frac{v_{\rm CSM}}{200\,{\rm km\,s}^{-1}}\right), \quad ({\rm B2})$$

which confirms the super-Eddington mass-transfer rate.[23] As a cross check, we can also roughly infer $\dot{M}$ from the observed SN. The collision of the SN with the CSM generates a shock that powers the SN light curve. The kinetic energy dissipation rate is

$$L_{\rm kin} = 2\pi r^2\left(\frac{\dot{M}}{4\pi r^2 v_{\rm CSM}}\right)v_{\rm sh}^3 \sim 5.5\times 10^{43}\,{\rm erg\,s}^{-1}\left(\frac{\dot{M}}{0.1 M_\odot\,{\rm yr}^{-1}}\right) \times\left(\frac{v_{\rm CSM}}{200\,{\rm km\,s}^{-1}}\right)^{-1}\left(\frac{v_{\rm sh}}{7000\,{\rm km\,s}^{-1}}\right)^{3} \quad ({\rm B3})$$

where $v_{\rm sh}$ is the forward shock velocity. Assuming that the luminosity at the second peak is generated by the interaction with CSM generated in the precursor phase, we infer a mass-loss rate of

$$\dot{M} \sim 2\times 10^{-2}\,M_\odot\,{\rm yr}^{-1}\epsilon^{-1}\left(\frac{L_{\rm rad}}{10^{43}\,{\rm erg\,s}^{-1}}\right) \times\left(\frac{v_{\rm CSM}}{200\,{\rm km\,s}^{-1}}\right)\left(\frac{v_{\rm sh}}{7000\,{\rm km\,s}^{-1}}\right)^{-3}, \quad ({\rm B4})$$

where $\epsilon = L_{\rm rad}/L_{\rm kin}\leqslant 1$ is the radiation conversion efficiency. While this estimate is quite sensitive to the assumed $v_{\rm sh}$, it implies that a similarly high $\dot{M}$ is also required to explain the SN. The required mass-transfer rate of $\sim$0.02–0.2$M_\odot\,{\rm yr}^{-1}$ for $\epsilon\approx 0.1$–1 roughly overlaps with the range obtained from simulations of binaries composed of a low-mass (2.5–3 $M_\odot$) He star and a neutron star, years to decades before the SN (S. C. Wu & J. Fuller 2022, Figure 2).

Appendix C
Spectroscopic Observations

Table C1 shows a log of the spectroscopic observations of SN 2023fyq and SN 2019kbj.

---

[23] As the blackbody temperature is $\sim 10^4$ K during the precursor phase, even for $\dot{M} \gtrsim \dot{M}_{\rm min}$, we expect that the blackbody radius would not be too much larger than the observed value. This is because the temperature drops as a function of radius, and the opacity at $r > R_{\rm BB}$ will rapidly drop with radius due to helium recombination (analogous to the recombination front of SN II-P).

Table C1
Spectroscopic Observations of SN 2023fyq and SN 2019kbj

Object	UT Date	Julian Date (days)	Phase (days)	Telescope	Instrument	$R(\lambda/\Delta_\lambda)$
SN 2023fyq	2023-07-27	2460152.743	−1.6	Gemini	GMOS	1680
SN 2023fyq	2023-07-27	2460152.850	−1.4	FTS	FLOYDS	400–700
SN 2023fyq	2023-07-28	2460153.859	−0.4	FTS	FLOYDS	400–700
SN 2023fyq	2023-07-31	2460156.851	2.6	FTS	FLOYDS	400–700
SN 2023fyq	2023-08-01	2460157.740	3.4	Gemini	GMOS	1300
SN 2023fyq	2023-08-04	2460160.858	6.6	FTS	FLOYDS	400–700
SN 2023fyq	2023-08-04	2460161.392	7.1	NOT	ALFOSC	400
SN 2023fyq	2023-12-12	2460291.123	136.8	Keck	LRIS	750–1475
SN 2023fyq	2024-01-23	2460332.761	178.5	SOAR	GHTS	1850
SN 2023fyq	2024-03-11	2460380.865	226.6	LBT	MODS	2300
SN 2023fyq	2024-05-01	2460431.943	277.6	Keck	LRIS	750–1475
SN 2019kbj	2019-09-23	2458750.817	80	Keck	DEIMOS	1875

Note. Faulkes Telescope South.

ORCID iDs

Yize Dong (董一泽) https://orcid.org/0000-0002-7937-6371
Daichi Tsuna https://orcid.org/0000-0002-6347-3089
Stefano Valenti https://orcid.org/0000-0001-8818-0795
David J. Sand https://orcid.org/0000-0003-4102-380X
Jennifer E. Andrews https://orcid.org/0000-0003-0123-0062
K. Azalee Bostroem https://orcid.org/0000-0002-4924-444X
Griffin Hosseinzadeh https://orcid.org/0000-0002-0832-2974
Emily Hoang https://orcid.org/0000-0003-2744-4755
Saurabh W. Jha https://orcid.org/0000-0001-8738-6011
Daryl Janzen https://orcid.org/0000-0003-0549-3281
Jacob E. Jencson https://orcid.org/0000-0001-5754-4007
Michael Lundquist https://orcid.org/0000-0001-9589-3793
Darshana Mehta https://orcid.org/0009-0008-9693-4348
Aravind P. Ravi https://orcid.org/0000-0002-7352-7845
Nicolas E. Meza Retamal https://orcid.org/0000-0002-7015-3446
Jeniveve Pearson https://orcid.org/0000-0002-0744-0047
Manisha Shrestha https://orcid.org/0000-0002-4022-1874
Alceste Z. Bonanos https://orcid.org/0000-0003-2851-1905
D. Andrew Howell https://orcid.org/0000-0003-4253-656X
Nathan Smith https://orcid.org/0000-0001-5510-2424
Joseph Farah https://orcid.org/0000-0003-4914-5625
Daichi Hiramatsu https://orcid.org/0000-0002-1125-9187
Curtis McCully https://orcid.org/0000-0001-5807-7893
Estefania Padilla Gonzalez https://orcid.org/0000-0003-0209-9246
Emmanouela Paraskeva https://orcid.org/0000-0003-2814-4383
Craig Pellegrino https://orcid.org/0000-0002-7472-1279
Giacomo Terreran https://orcid.org/0000-0003-0794-5982
Joshua Haislip https://orcid.org/0000-0002-6703-805X
Vladimir Kouprianov https://orcid.org/0000-0003-3642-5484
Daniel E. Reichart https://orcid.org/0000-0002-5060-3673

References

Andrews, J. E., & Smith, N. 2018, MNRAS, 477, 74
Arnett, W. D. 1982, ApJ, 253, 785
Astropy Collaboration, Price-Whelan, A. M., Lim, P. L., et al. 2022, ApJ, 935, 167
Astropy Collaboration, Price-Whelan, A. M., Sipőcz, B. M., et al. 2018, AJ, 156, 123
Astropy Collaboration, Robitaille, T. P., Tollerud, E. J., et al. 2013, A&A, 558, A33
Becker, A., 2015 HOTPANTS: High Order Transform of PSF ANd Template Subtraction, ascl:1504.004
Bellm, E. C., Kulkarni, S. R., Graham, M. J., et al. 2019, PASP, 131, 018002
Ben-Ami, T., Arcavi, I., Newsome, M., et al. 2023, ApJ, 946, 30
Bertin, E., Mellier, Y., Radovich, M., et al. 2002, in ASP Conf. Ser. 281, Astronomical Data Analysis Software and Systems XI, ed. D. A. Bohlender, D. Durand, & T. H. Handley (San Francisco, CA: ASP), 228
Bianco, F. B., Ivezić, Ž., Jones, R. L., et al. 2022, ApJS, 258, 1
Blagorodnova, N., Kotak, R., Polshaw, J., et al. 2017, ApJ, 834, 107
Blondin, S., & Tonry, J. L. 2007, ApJ, 666, 1024
Bradley, L., Sipőcz, B., Robitaille, T., et al. 2022, astropy/photutils, v1.5.0, Zenodo, doi:10.5281/zenodo.6825092
Breeveld, A. A., Landsman, W., Holland, S. T., et al. 2011, in AIP Conf. Ser. 1358, Gamma Ray Bursts 2010, ed. J. E. McEnery, J. L. Racusin, & N. Gehrels (Melville, NY: AIP), 373
Brennan, S. J., Sollerman, J., Irani, I., et al. 2024, A&A, 684, L18
Brown, T. M., Baliber, N., Bianco, F. B., et al. 2013, PASP, 125, 1031
Chen, P., Gal-Yam, A., Sollerman, J., et al. 2024, Natur, 625, 253
Chevalier, R. A. 1982, ApJ, 258, 790
Chevalier, R. A. 2012, ApJL, 752, L2
Clemens, J. C., Crain, J. A., & Anderson, R. 2004, Proc. SPIE, 5492, 331
De, K. 2023, TNSCR, 825 1
De, K., Kasliwal, M. M., Ofek, E. O., et al. 2018, Sci, 362, 201
Demianenko, M., Malanchev, K., Samorodova, E., et al. 2023, A&A, 677, A16
Dessart, L., Hillier, D. J., & Kuncarayakti, H. 2022, A&A, 658, A130
Ertl, T., Woosley, S. E., Sukhbold, T., & Janka, H. T. 2020, ApJ, 890, 51
Faber, S. M., Phillips, A. C., Kibrick, R. I., et al. 2003, Proc. SPIE, 4841, 1657
Filippenko, A. V., Matheson, T., & Ho, L. C. 1993, ApJL, 415, L103
Foley, R. J., Smith, N., Ganeshalingam, M., et al. 2007, ApJL, 657, L105
Foreman-Mackey, D., Hogg, D. W., Lang, D., & Goodman, J. 2013, PASP, 125, 306
Fox, O. D., & Smith, N. 2019, MNRAS, 488, 3772
Fryer, C. L., Belczynski, K., Berger, E., et al. 2013, ApJ, 764, 181
Fryer, C. L., & Woosley, S. E. 1998, ApJL, 502, L9
Fukugita, M., Ichikawa, T., Gunn, J. E., et al. 1996, AJ, 111, 1748
Fuller, J. 2017, MNRAS, 470, 1642
Fuller, J., & Ro, S. 2018, MNRAS, 476, 1853
Gal-Yam, A., & Leonard, D. C. 2009, Natur, 458, 865
Gal-Yam, A., Leonard, D. C., Fox, D. B., et al. 2007, ApJ, 656, 372
Gangopadhyay, A., Misra, K., Hiramatsu, D., et al. 2020, ApJ, 889, 170
Gehrels, N., Chincarini, G., Giommi, P., et al. 2004, ApJ, 611, 1005
Graham, M. J., Kulkarni, S. R., Bellm, E. C., et al. 2019, PASP, 131, 078001
Graham, M. L., Kennedy, T. D., Kumar, S., et al. 2022, MNRAS, 511, 3682
Harris, C. R., Millman, K. J., van der Walt, S. J., et al. 2020, Natur, 585, 357
Hiramatsu, D., Matsumoto, T., Berger, E., et al. 2024, ApJ, 964, 181
Ho, A. Y. Q., Perley, D. A., Gal-Yam, A., et al. 2023, ApJ, 949, 120
Hook, I. M., Jørgensen, I., Allington-Smith, J. R., et al. 2004, PASP, 116, 425
Hosseinzadeh, G., Arcavi, I., Valenti, S., et al. 2017, ApJ, 836, 158
Hosseinzadeh, G., & Gomez, S. 2020, Light Curve Fitting, v0.2.0, Zenodo, doi:10.5281/zenodo.4312178
Hosseinzadeh, G., McCully, C., Zabludoff, A. I., et al. 2019, ApJL, 871, L9
Hunter, D. J., Valenti, S., Kotak, R., et al. 2009, A&A, 508, 371

Hunter, J. D. 2007, CSE, 9, 90

Itagaki, K. 2023, TNSAN, 216, 1

Jiang, B., Jiang, S., & Ashley Villar, V. 2020, RNAAS, 4, 16

Karamehmetoglu, E., Taddia, F., Sollerman, J., et al. 2017, A&A, 602, A93

Kashiyama, K., Sawada, R., & Suwa, Y. 2022, ApJ, 935, 86

Kleiser, I. K. W., & Kasen, D. 2014, MNRAS, 438, 318

Kochanek, C. S., Shappee, B. J., Stanek, K. Z., et al. 2017, PASP, 129, 104502

Könyves-Tóth, R., Vinkó, J., Ordasi, A., et al. 2020, ApJ, 892, 121

Lang, D., Hogg, D. W., Mierle, K., Blanton, M., & Roweis, S. 2010, AJ, 139, 1782

Leung, S.-C., & Fuller, J. 2020, ApJ, 900, 99

Leung, S.-C., Nomoto, K., & Blinnikov, S. 2019, ApJ, 887, 72

Liu, Y.-Q., Modjaz, M., Bianco, F. B., & Graur, O. 2016, ApJ, 827, 90

Lu, W., Fuller, J., Quataert, E., & Bonnerot, C. 2023, MNRAS, 519, 1409

Lyman, J. D., Bersier, D., James, P. A., et al. 2016, MNRAS, 457, 328

MacLeod, M., Ostriker, E. C., & Stone, J. M. 2018, ApJ, 863, 5

Margalit, B. 2022, ApJ, 933, 238

Masci, F. 2011, Computing Flux Upper-limits for Non-detections, https://web.ipac.caltech.edu/staff/fmasci/home/mystats/UpperLimits_FM2011.pdf

Masci, F. J., Laher, R. R., Rusholme, B., et al. 2023, arXiv:2305.16279

Matheson, T., Filippenko, A. V., Chornock, R., Leonard, D. C., & Li, W. 2000, AJ, 119, 2303

Matzner, C. D., & Ro, S. 2021, ApJ, 908, 23

Mauerhan, J. C., Smith, N., Filippenko, A. V., et al. 2013, MNRAS, 430, 1801

Mauerhan, J. C., Van Dyk, S. D., Graham, M. L., et al. 2015, MNRAS, 447, 1922

Maund, J. R., Pastorello, A., Mattila, S., Itagaki, K., & Boles, T. 2016, ApJ, 833, 128

McKinney, W. 2010, in Proc. of the 9th Python in Science Conf., ed. S. van der Walt & J. Millman (Austin, TX: SciPy), 56

Metzger, B. D. 2022, ApJ, 932, 84

Metzger, B. D., & Pejcha, O. 2017, MNRAS, 471, 3200

Modjaz, M., Gutierrez, C. P., & Arcavi, I. 2019, NatAs, 3, 717

Modjaz, M., Li, W., Butler, N., et al. 2009, ApJ, 702, 226

Moore, T., Smartt, S. J., Nicholl, M., et al. 2023, ApJL, 956, L31

Morozova, V., Piro, A. L., Fuller, J., & Van Dyk, S. D. 2020, ApJL, 891, L32

Munari, U., & Zwitter, T. 1997, A&A, 318, 269

Ofek, E. O., Sullivan, M., Cenko, S. B., et al. 2013, Natur, 494, 65

Ofek, E. O., Sullivan, M., Shaviv, N. J., et al. 2014, ApJ, 789, 104

Oke, J. B., Cohen, J. G., Carr, M., et al. 1995, PASP, 107, 375

Pastorello, A., Benetti, S., Brown, P. J., et al. 2015c, MNRAS, 449, 1921

Pastorello, A., Cappellaro, E., Inserra, C., et al. 2013, ApJ, 767, 1

Pastorello, A., Kochanek, C. S., Fraser, M., et al. 2018, MNRAS, 474, 197

Pastorello, A., Mattila, S., Zampieri, L., et al. 2008b, MNRAS, 389, 113

Pastorello, A., Prieto, J. L., Elias-Rosa, N., et al. 2015b, MNRAS, 453, 3649

Pastorello, A., Quimby, R. M., Smartt, S. J., et al. 2008a, MNRAS, 389, 131

Pastorello, A., Smartt, S. J., Mattila, S., et al. 2007, Natur, 447, 829

Pastorello, A., Tartaglia, L., Elias-Rosa, N., et al. 2015a, MNRAS, 454, 4293

Pastorello, A., Wang, X. F., Ciabattari, F., et al. 2016, MNRAS, 456, 853

Pejcha, O. 2014, ApJ, 788, 22

Pejcha, O., Metzger, B. D., & Tomida, K. 2016, MNRAS, 455, 4351

Pellegrino, C., Howell, D. A., Vinkó, J., et al. 2022, ApJ, 926, 125

Perley, D. A. 2019, PASP, 131, 084503

Pogge, R. 2019, rwpogge/modsCCDRed 2.0, 2.0, Zenodo, doi:10.5281/zenodo.2550741

Pogge, R. W., Atwood, B., Brewer, D. F., et al. 2010, Proc. SPIE, 7735, 77350A

Poznanski, D., Prochaska, J. X., & Bloom, J. S. 2012, MNRAS, 426, 1465

Prentice, S. J., Maguire, K., Boian, I., et al. 2020, MNRAS, 499, 1450

Prochaska, J., Hennawi, J., Westfall, K., et al. 2020, JOSS, 5, 2308

Prochaska, J. X., Hennawi, J., Cooke, R., et al. 2020, pypeit/PypeIt: Release 1.0.0, v1.0.0, Zenodo, doi:10.5281/zenodo.3743493

Quataert, E., & Shiode, J. 2012, MNRAS, 423, L92

Renzo, M., Farmer, R., Justham, S., et al. 2020, A&A, 640, A56

Sanders, N. E., Soderberg, A. M., Foley, R. J., et al. 2013, ApJ, 769, 39

Schlafly, E. F., & Finkbeiner, D. P. 2011, ApJ, 737, 103

Schlafly, E. F., Finkbeiner, D. P., Schlegel, D. J., et al. 2010, ApJ, 725, 1175

Schrøder, S. L., MacLeod, M., Loeb, A., Vigna-Gómez, A., & Mandel, I. 2020, ApJ, 892, 13

Science Software Branch at STScI, 2012 PyRAF: Python Alternative for IRAF, Astrophysics Source Code Library, record ascl:1207.011

Shappee, B. J., Prieto, J. L., Grupe, D., et al. 2014, ApJ, 788, 48

Shingles, L., Smith, K. W., Young, D. R., et al. 2021, TNSAN, 7, 1

Shiode, J. H., & Quataert, E. 2014, ApJ, 780, 96

Shivvers, I., Zheng, W., Van Dyk, S. D., et al. 2017, MNRAS, 471, 4381

Smith, K. W., Smartt, S. J., Young, D. R., et al. 2020, PASP, 132, 085002

Smith, N. 2014, ARA&A, 52, 487

Smith, N. 2017, in Handbook of Supernovae, ed. A. W. Alsabti & P. Murdin (Berlin: Springer), 403

Smith, N., & Andrews, J. E. 2020, MNRAS, 499, 3544

Smith, N., Andrews, J. E., Milne, P., et al. 2024, MNRAS, 530, 405

Smith, N., Andrews, J. E., Van Dyk, S. D., et al. 2016, MNRAS, 458, 950

Smith, N., & Arnett, W. D. 2014, ApJ, 785, 82

Smith, N., Foley, R. J., & Filippenko, A. V. 2008, ApJ, 680, 568

Smith, N., & McCray, R. 2007, ApJL, 671, L17

Smith, N., Miller, A., Li, W., et al. 2010, AJ, 139, 1451

Smith, N., Mauerhan, J. C., Cenko, S. B., et al. 2015, MNRAS, 449, 1876

Soker, N. 2013, arXiv:1302.5037

Soker, N. 2019, SCPMA, 62, 119501

Soker, N. 2024, Galax, 12, 33

Soker, N., & Tylenda, R. 2003, ApJL, 582, L105

Strotjohann, N. L., Ofek, E. O., Gal-Yam, A., et al. 2021, ApJ, 907, 99

Tartaglia, L., Pastorello, A., Sullivan, M., et al. 2016, MNRAS, 459, 1039

Tartaglia, L., Sand, D. J., Valenti, S., et al. 2018, ApJ, 853, 62

Thöne, C. C., de Ugarte Postigo, A., Fryer, C. L., et al. 2011, Natur, 480, 72

Tonry, J. L. 2011, PASP, 123, 58

Tonry, J. L., Denneau, L., Heinze, A. N., et al. 2018, PASP, 130, 064505

Torres, S., Briceño, C., & Quint, B. 2017, Goodman HTS Pipeline Documentation 1.3.6, https://soardocs.readthedocs.io/projects/goodman-pipeline/

Tsuna, D., Matsumoto, T., Wu, S. C., & Fuller, J. 2024a, ApJ, 966, 30

Tsuna, D., Takei, Y., & Shigeyama, T. 2023, ApJ, 945, 104

Tsuna, D., Wu, S. C., Fuller, J., Dong, Y., & Piro, A. L. 2024b, OJAp, 7, 82

Tsvetkov, D. Y., Volkov, I. M., & Pavlyuk, N. N. 2015, IBVS, 6140, 1

Tully, R. B., Courtois, H. M., & Sorce, J. G. 2016, AJ, 152, 50

Tylenda, R., Hajduk, M., Kamiński, T., et al. 2011, A&A, 528, A114

Valenti, S., Benetti, S., Cappellaro, E., et al. 2008, MNRAS, 383, 1485

Valenti, S., Howell, D. A., Stritzinger, M. D., et al. 2016, MNRAS, 459, 3939

Valenti, S., Sand, D., Pastorello, A., et al. 2014, MNRAS, 438, L101

Valerin, G., Benetti, S., Elias-Rosa, N., et al. 2023, TNSCR, 1777 1

Virtanen, P., Gommers, R., Oliphant, T. E., et al. 2020, NatMe, 17, 261

Wangq, Q., Goel, A., Dessart, L., et al. 2024, MNRAS, 530, 3906

Woosley, S. E. 2017, ApJ, 836, 244

Woosley, S. E. 2019, ApJ, 878, 49

Woosley, S. E., Blinnikov, S., & Heger, A. 2007, Natur, 450, 390

Wu, S. C., & Fuller, J. 2022, ApJL, 940, L27

Yang, S., Sand, D. J., Valenti, S., et al. 2019, ApJ, 875, 59

Yao, Y., De, K., Kasliwal, M. M., et al. 2020, ApJ, 900, 46

Yaron, O., & Gal-Yam, A. 2012, PASP, 124, 668

Yoshida, T., Umeda, H., Maeda, K., & Ishii, T. 2016, MNRAS, 457, 351

Young, D. 2022, Plot Results from ATLAS Force Photometry Service, https://gist.github.com/thespacedoctor/86777fa5a9567b7939e8d84fd8cf6a76

Yuan, F., & Narayan, R. 2014, ARA&A, 52, 529

Zhang, W., & Fryer, C. L. 2001, ApJ, 550, 357